Published in final edited form as:

ACS Appl Mater Interfaces. 2021 September 01; 13(34): 40214–40228. doi:10.1021/acsami.1c03504.

Gold nanorod enhanced Photoacoustic Microscopy and Optical Coherence Tomography of Choroidal Neovascularization

Van-Phuc Nguyen[1], **Yanxiu Li**[1], **Jessica Henry**[1], **Wei Zhang**[2], **Xueding Wang**[2,*], **Yannis M Paulus**[1,2,*]

[1]Department of Ophthalmology and Visual Sciences, University of Michigan, Ann Arbor, MI 48105, USA

[2]Department of Biomedical Engineering, University of Michigan, Ann Arbor, MI 48105, USA

Abstract

Visualization and evaluation of choroidal neovascularization (CNV) is a major challenge to improve treatment outcomes for patients with age-related macular degeneration (AMD). Limitations of current imaging techniques include limited penetration depth, spatial resolution, sensitivity, and difficulty visualizing CNV from the healthy microvasculature. In this study, a custom-built multimodal photoacoustic microscopy (PAM) and optical coherence tomography (OCT) system was developed to distinguish the margin of CNV in living rabbits with the assistance of functionalized gold nanorods conjugating with RGD ligands (GNR-RGD). Intravenous administration of GNR-RGD into rabbits with a CNV model resulted in signal enhancement of 27.2-fold in PAM and 171.4% in OCT. This molecular imaging technique of contrast-enhanced PAM and OCT is a promising tool for precise imaging of CNV as well as evaluation of the pathophysiology *in vivo* without destruction of tissue.

Keywords

Photoacoustic microscopy; optical coherence tomography; choroidal neovascularization; contrast agents; multimodal molecular imaging; gold nanorods; photoacoustic ophthalmoscopy

*Corresponding Authors: Yannis M. Paulus, M.D., F.A.C.S., Department of Ophthalmology and Visual Sciences Department of Biomedical Engineering, University of Michigan 1000 Wall Street, Ann Arbor, MI 48105, USA, ypaulus@med.umich.edu, Xueding Wang, Ph.D., Department of Biomedical Engineering Department of Radiology, University of Michigan, xdwang@umich.edu.

Author Contributions

V.P.N., implemented tissue culture and analysis, designed the experiments and employed animal models, *in vitro* characterization and *in vivo* PAM and OCT imaging experiments, maintenance the custom imaging system, rendering three-dimensional volumetric visualization of PAM data using Amira software, and wrote of the manuscript. Y.L. assisted with animal models. J.H. helped *in vitro* study and histopathological analysis. W.Z contributed with data analysis. X. W. was responsible for evaluation of the data and assisted with preparation of the manuscript. Y.M.P directed the project and wrote the manuscript. All authors participated in critical evaluation of the data, discussions of the results, and critical revision of the manuscript.

Supporting Information Available: The following files are available free of charge. Supplementary Information Gold Nanorods Contrast Enhanced PAM and OCT.docx

Transmission electron microscopy (TEM). Confocal laser scanning microscopic images of cells treated with GNR without conjugation with RGD. *In vivo* longitudinal PAM acquired at 578 and 700 nm. *In vivo* PAM images of CNV pre and post injection of GNRs without RGD. Region of interest (ROI) analysis to quantify OCT signal.

Competing interests

The authors declare that they have no competing interests.

Introduction

Age-related macular degeneration (AMD) is a leading cause of vision impairment and blindness worldwide. In according to WHO, an estimated 288 million people will be diagnosed with AMD in 2040, accounting for 8.7% of blindness[1]. AMD can be classified into two groups: dry (degenerative) AMD and wet (neovascular) AMD. More than 90% of patients with AMD have dry AMD[2], but wet AMD causes the majority of patients with blindness[3]. In wet AMD, newly developed neovascularization from the choroidal layer breaks through Bruch's membrane and grow in the subretinal layer, named choroidal neovascularization (CNV)[4]. CNV are unstructured, leaky vessels. CNV is usually diagnosed using fluorescein angiography (FA), fluorescence lifetime imaging ophthalmoscopy, indocyanine green angiography (ICGA), optical coherence tomography (OCT), and OCT angiography (OCTA)[5–9]. These imaging techniques provide valuable diagnostic information of CNV. For example, FA and ICGA allow identification of the position of CNV based on leakage. However, both FA and ICGA imaging have limited penetration depth. OCT and OCTA offer visualization of the pathologic vascular network in both two-dimensional and three- dimensional perspectives with high resolution. However, OCT and OCTA have a limited classification of the choroid and limited capability to achieve molecular imaging due to the strong scattering background signal for molecular imaging. These imaging modalities have difficulty penetrating to the deeper choroid layer to image with high contrast and high resolution choroidal vasculature and provide limited choroidal biomarkers of disease. Therefore, there is an unmet need for molecular imaging methods that can identify CNV.

Photoacoustic microscopy (PAM) is a hybrid optical and acoustic imaging method[10–12]. Photoacoustic images are created based on the acoustic wave generated from the absorption of short pulsed laser light by chromophores in biological tissues such as hemoglobin, melanin, and lipid. Due to relatively lower scattering and attenuation of the acoustic wave in biological tissues compared to the light, PAM has the capability to offer micron-level spatial resolution at penetration depths of a few millimeters[10]. In addition, besides describing tissue anatomy, the optical contrast presented by PAM is highly sensitive to the functional and molecular information in biological samples. Due to these great aspects, PAM holds promise for many preclinical and clinical applications such as ophthalmology.

For applications in ophthalmology, PAM has been integrated with OCT, SLO, and fluorescence microscopy to combine the benefits of each imaging modality. Theses multimodality imaging systems have been extensively explored for identification of retinal vessels (RVs)[13], choroidal vessels (CVs)[14], retinal pigment epithelium (RPE) cells[15–17], melanin[18], corneal neovascularization[19], retinal neovascularization (RNV)[20,21], laser-induced injury[22], retinal vein occlusion[23–26], and choroidal neovascularization (CNV) in rodents (*e.g.* mice and rats) and large animal eyes (*e.g.* rabbits)[27–29,13,24,30,31]. In previous studies, our group has reported a multimodal PAM and OCT imaging system to visualize RVs, CVs, RNV, and CNV with high resolution and high contrast[13,21,24,26,32]. However, these healthy and abnormal vasculatures were visualized based on the endogenous optical contrast between hemoglobin and other tissues. While there is no optical contrast between newly developed vessels and the surrounding established normal microvasculature,

it is difficult to distinguish them. A study by Nguyen *et al.* applied semi- automated segmentation to distinguish RNV[20,24]. While this method has shown the capability to distinguish RNV from adjacent normal microvasculature, it is computationally time-consuming and not always accurate in isolating abnormal neovascularization. To better distinguish neovascularization from surrounding normal microvasculature, several NIR exogenous contrast agents, including gold nanoparticles, silver nanoparticles, single-wall carbon nanotubes, dye-based contrast agents (indocyanine green, methylene blue, Prussian blue, and IR780), naphthalocyanine, semiconductor polymers, or gene reporters[33–36], have been used to enhance the optical absorption contrast. The contrast agents did not specifically target the molecular biomarkers of neovascularization in these previous studies. In addition, in these previous studies, the contrast agents were solely employed to enhance the optical absorption contrast for photoacoustic imaging, while their potential in enhancing the optical scattering contrast for OCT was not explored.

Due to their strong optical absorption and superb optical scattering as well as other advantages such as great biocompatibility and minimal cytotoxicity, plasmonic gold nanoparticles (GNPs) are widely used as contrast agents to enhance PA signal and OCT signal. In previous studies[37,38], GNPs were applied in PAM and OCT to improve the visualization of vasculature. For example, in a study by Nguyen *et al.*[38], it was shown that intravenous injection of spherical gold nanoparticles (SNPs) led to PA signal enhancement by 82% and OCT signal enhancement by 47%. One limitation of this study was that the peak absorption of SNPs overlapped with the peak absorption of hemoglobin, which limited the contrast enhancement in biological tissues. In addition, the OCT signal was only mildly increased due to the relatively weak scattering of the SNPs in the visible spectrum. To achieve optimal performance *in vivo*, a number of characteristics of SNPs, such as size, shape, and surface modification, need to be adjusted so that strong contrast enhancement, specific targeting, and reduced toxicity can be possible. Particularly, it is desired that, by modifying the morphology of the GNPs, their plasmonic peak absorption can be shifted from the visible region to the NIR region where the intrinsic optical absorption from the native chromophores is significantly weaker, increasing the sensitivity for molecular imaging. With that in mind, gold nanostars, gold nanorods (GNR), and gold nanocubes were designed and tested [39– 42,43]. Recently, a report by Liba *et al.* has described that large GNRs produce OCT signal more efficiently than small GNRs with similar aspect ratios[44]. The authors showed that OCT signal was enhanced about 110 times with the use of GNRs with width of 132 nm and length of 107 nm when compared to that using smaller GNRs with width of 15 nm and length of 50 nm. In another study, Chen *et al.* have described that smaller GNRs with size of 8 nm by 49 nm could produce 3.5-fold higher PA signal than larger GNRs with size of 18 nm by 120 nm. In addition, GNR have been explored as biocompatible PA contrast agents for imaging of cancer, lymph nodes, and stem cells[45]. All these evidences imply that GNR is an excellent optical contrast agent for both PAM and OCT.

In this study, for the first time to the best of our knowledge, GNRs are explored as a dual PAM and OCT molecular imaging contrast agent for *in vivo* ophthalmic applications. By conjugating GNRs with Arginine–Glycine–Aspartic (RGD) peptides, GNR-RGD can specifically target $\alpha v\beta 3$ integrin or other molecules overexpressed in CNV in the eye.

Molecular imaging using GNR-RGD was examined on two different clinically-relevant CNV rabbit models: 1) laser- induced retinal vein occlusion, and 2) subretinal injection of human vascular endothelial growth factor (VEGF-165) mixed with Matrigel. The experimental results *in vivo* demonstrated that functionalized GNR-RGD can enhance both optical absorption for PAM and optical scattering for OCT. With the signal enhancement specifically in neovascularization, both PAM and OCT were able to distinguish CNV from the surrounding normal microvasculature. The combination of high imaging resolution and high sensitivity to molecular biomarkers facilitated by PAM and OCT imaging powered by the GNR-RGD, as demonstrated in this study, offers a potential and practical tool to visualize and characterize neovascularization in the eye *in vivo*.

Results/Discussion

Characterization of the functionalized GNRs:

GNRs conjugated with molecular targeting RGD peptides were reported in previous studies[46,47]. The surface of GNRs were modified with polyethylene glycol (PEG) to increase the circulation of GNRs in the bloodstream and enhanced permeability and retention effect (EPR). Several studies have reported that PEG could prolong the half-life of GNR nanoparticles up to 19 hours after intravenous injection and exhibited 76 times longer than that of non-PEGylated GNRs (~ 15 min in blood)[48]. In addition, PEG could enhance the extravasation of GNPs at neovascularization due to the EPR effect[49]. In order to target choroidal neovascularization (CNV), RGD peptides were used to allow the synthesized GNRs to bind with integrin $\alpha v\beta 3$ and other integrins expressed in CNV. The morphology of GNR was observed using transmission electron microscopy (TEM) analysis (Fig. 1a). The inlet image in Fig. 1a shows a single GNR. In addition, the TEM images also confirmed that GNR-RGD has great stability without any obvious sign of aggregation over a time period of 4 weeks (Figure S1). The particle size distribution was measured from 250 nanoparticles on TEM images using ImageJ and DLS analysis as presented in Fig. 1b–d. The average size of GNRs was estimated to be 34.17 ± 4.85 nm in width and 103.28 ± 12.07 nm in length. Furthermore, the estimated particles size measured from DLS was 113 nm with disperse index of 0.5. This result is not significantly different from the particle sized obtained by TEM. The GNRs have a large negative charge with a zeta potential value of – 42.0 mV. Figure 1e shows the absorption spectrum of GNRs with a peak at 700 nm. This peak was selected as the excitation wavelength for the entire *in vivo* PAM experiments. Figure 1f shows the absorption spectrum of GNRs measured at different times over a period of 1 month. The graph shows minimal changes in the absorption spectrum, indicating that GNR were stable and suitable for *in vivo* experiments. To evaluate the photostability of GNR, five samples containing GNRs were illuminated with 80,000 short laser pulses at different energies of 40, 80, 160, 320, and 640 nJ. The absorption spectrum of the samples after laser irradiation did not change significantly, illustrating that GNRs have good photostability (Fig. 1g). A graph of TGA spectrum as a function of temperature of GNR-RGD shows a significant weight loss of the content of compound on the GNR-RGD with temperature (Fig. 1h). The sample's weight slightly reduced about 2% at 170 °C and then rapidly decreased at the temperature ranging from 200–350 °C due to decomposition of the organic compounds such as RGD and PEG. This indicated that the compounds used to functionalize GNRs were

completely degraded. The TGA curve also show that the total weight loss of the GNR-RGD was estimated to be 32% at highest temperature of 700 °C. This implies that the total weight of the nanoparticles was 68 %. Figure 1i illustrates a graph of the Fourier transformed infrared spectroscopy (FTIR) of polyethylene glycol (PEG 2k-SH), RGD, bare GNRs, and GNR-RGD. This result confirms the presence of functional PEG group and RGD peptide on the surface of GNR-RGD. In addition, the FTIR spectrum of GNR-RGD sample exhibited all characteristic peaks that could be found in PEG and RGD.

Cytotoxicity and cellular uptake of GNR-RGD.

Figure 2a–c show the viability of HeLa, BRECs, and b.End3 cells after treatment with GNRs at various concentrations (*i.e.*, 12.5, 25, 50, 100, 200, 400 and 500 μg/mL), and incubation times (24 h and 48 h). Overall, the percentages of cell viability were high and achieved more than 96% for HeLa (Fig. 2a), 95 % for BRECs (Fig. 2b), and 93 % for b.End 3 (Fig. 2c) cells even with treatment at a high concentration of 400 μg/mL GNRs and long incubation time of 48 h. These results were quite similar to that of the control (untreated cells), revealing that GNR-RGD induced minimal toxicity and did not impact the proliferative potential of the cells at the treated concentrations. The potential apoptosis induced by GNR-RGD was analyzed using Annexin-V FITC and PI apoptotic detection kit (Fig. 2d–f). Total apoptotic cells were estimated to be 5% and 6.7%, after incubation the BRECs cells without GNR-RGD (Fig. 2d) and with GNR-RGD (Fig. 2e) at concentration of 400 μg/mL for 24 h, respectively. The proportion of apoptotic cells was slightly increased after treated cells with GNRs at the same concentration after incubation time of 48 h (Fig. 2f). The result reveals that the total apoptotic cells were approximately 7.7%. This evidence shows that GNR-RGD induced minimal toxicity to the evaluated cells.

Figure 2g–j shows the targeting GNR-RGD were internalized in BRECs cells over an incubation of 24 h. Confocal laser scanning microscope images were acquired at different focal depths verified that GNR-RGD were internalized and distributed at different locations in the cells (see supplementary video visualization 1). Fluorescent red color indicates the position of the internalized GNRs (Fig. 2h–j). In contrast, GNR without conjugation with RGD were not internalized well in cells, as shown in supplementary Figure S2. The higher incubation of GNR- RGD concentrations, the more GNR-RGD uptake by the cells. Note that the cell nuclei were stained with blue fluorescent color by DAPI. Although the internalized GNR-RGD could be visualized by confocal microscopy, these nanoparticles were further examined using our PAM imaging. Figure 2k–n shows PAM images of the cells acquired at an excitation wavelength of 700 nm. At a concentration of 100 μg/mL, the internalized GNR-RGD were clearly visualized on the PAM with high signal to noise ratio due to the strong absorption of laser light by the GNRs within the cells (Fig. 2n). On the contrary, less PAM contrast was observed on the sample treated with lower concentration of GNRs (25 μg/mL) as shown in Fig. 2l. By measuring the PA amplitude produced by the GNRs within the cells, the PAM signal increased by 14.2 and 1.4-fold for the highest concentration of 100 μg/mL and the lowest concentration of 25 μg/mL when compared to background, respectively (*i.e.*, PAsignal= 1.85 ± 0.05 a.u. for 100 μg/mL, PAsignal = 1.34 ± 0.06 a.u. for 25 μg/mL and PAsignal= 0.13 ± 0.02 a.u. for background).

In vitro PAM and OCT of GNR-RGD:

To evaluate the multimodal PAM and OCT contrast properties of GNR-RGD, phantoms filled with GNR-RGD at various concentrations (*i.e.*, 0 (saline), 0.005, 0.01, 0.02, 0.04 and 0.08 mg/mL) were prepared and imaged with the PAM and OCT imaging system. The PAM images of these phantoms were acquired using an excitation wavelength of 700 nm (Fig. 3a). The GNR-RGD produced strong PA signals, and all samples containing GNR-RGD were visible on PAM images. In contrast, sample poured with saline was not visible on the PAM, and the PA signal is equal to signal generated from the background noise. Note that the PA signal amplitude increases linearly with concentration of GNR-RGD ($R^2 = 0.99$) as shown in Fig. 3b. The sample containing 0.08 mg/mL of GNR-RGD produces 25.8-fold and 2.6-fold PA signal higher than that of control and the sample filled with 0.005 mg/mL of GNR- RGD (PAsignal = 250 ± 4.9 a.u. for 0.08 mg/mL, PAsignal = 25.6 ± 3.9 a.u. for 0.005 mg/mL, and PAsignal = 9.7 ± 2.1 a.u. for control). The lowest detectable concentration was 0.005 mg/mL. To evaluate photostability, a sample of GNRs was illuminated with 800,000 short laser pulses at an energy of 80 nJ. The recorded PA signal produced by GNRs was stable and did not change the absorption spectrum when compared to the sample without laser illumination (Fig. 3c).

To examine OCT contrast properties of GNR-RGD, a group of capillary glass tubes containing GNR-RGD at different concentrations were imaged with the OCT imaging system. GNR-RGD generated strong OCT signal, and all samples were clearly visible with high contrast (Fig. 3d). The control sample did not create OCT signal due to its low scattering of the incident light. The change in OCT signal in relation to GNR-RGD concentration was quantified and plotted (Fig. 3e). The OCT signal increased linearly with increasing GNR-RGD concentrations ($R^2 = 0.91$). At concentration of 0.08 mg/mL, the OCT signal of GNRs exhibited 40.5-fold higher than that of background (*i.e.*, OCTSignal = 40. 5 ± 1.9, and 1.0 ± 0.1 (a.u.) for GNR at 0.08 mg/mL, and background, respectively, $p < 0.05$). At lowest concentration of 0.005 mg/mL, GNR-RGD generated about 7.6-fold OCT signal enhancement when compared to background (OCTSignal = 7.6 ± 1.9(a.u.)).

In vivo PAM visualization of CNV:

The ability of GNR-RGD as a dual modality contrast agent was investigated in two different choroidal neovascularization (CNV) models in living rabbits, including RVO-induced CNV (N=3) and subretinal injection of VEGF-165 (N=3). 400 μL of GNR-RGD in PBS (2.5 mg/mL) was intravenously injected into each rabbit model via the marginal ear vein. In the RVO model, occluded retinal blood vessels induced hypoxia in the retinal tissues and the subsequent release of vascular endothelial growth factor (VEGF), leading to formation of the CNV. In addition, rabbits have a merangiotic retinal vasculature, unlike the holangiotic retinal vasculature in humans, and thus they possibly are more likely to develop CNV after RVO due to the lack of retinal vasculature within some of the ischemic regions and the necessity of angiogenesis to develop from existing vasculature. In the subretinal injection model, VEGF was directly injected into the subretinal space along with Matrigel. The Matrigel served as an efficient scaffold, trapped the growth factor in subretinal space, and allowed it to slowly release to form the CNV. The PAM images of CNV were acquired along with OCT, FA, and ICGA over time for a period of 14 days using the excitation

wavelength of 578 nm and 700 nm. The wavelength of 578 nm was used to detect retinal microvasculature due to strong optical absorption of hemoglobin at that wavelength. Figure 4 exhibits long-term PA visualization of CNV and the surrounding microvasculature pre- and post-injection of GNR-RGD *in vivo*. Figure 4a–d shows the color fundus photography and FA images. The fundus images show the major retinal and choroidal vessels and optic nerve. The FA image demonstrates the morphology of capillaries as well as identifying the position of CNV from the leakage of fluorescein dye on the late phase FA photos (white arrows). No PA image contrast was detected before the injection of GNR-RGD acquired at 700 nm due to low absorption of hemoglobin within blood vessels at that wavelength. Figure 4e– k exhibits 3D rendered and maximum intensity projection (MIP) PAM images from a top view (x– y) and front view (x–z) acquired at 24 h post-injection. The 3D PAM image shows strong PA signal generated by GNR-RGD accumulated at CNV, and the position of CNV was clearly differentiated from the adjacent normal microvasculature. The high contrast of retinal blood vessels was achieved at 578 nm due to strong absorption of blood at this wavelength. In contrast, there was minimal PA signal generated from the blood when a longer excitation wavelength of 700 nm was used where the PA signal was mainly generated by the strong-absorbing GNRs (Fig. 4g–j). The pseudo-yellow color represents the biodistribution of GNRs within the CNV.

Figure 4l shows longitudinal 3D volumetric PAM images acquired at different time points over a period of 28 days after-injection. These PAM images were acquired at two different wavelengths of 578 and 700 nm (Supplementary Figure S3) and overlaid on the same image plane. On the contrary, the animal injected with GNR without conjugation to RGD peptides caused a non-significant PA signal increase with rapid reduction at 4 h post injection (Fig. S4).

To visualize the location of the detected CNV and compare it to surrounding retinal and choroidal vessels, vasculature color-encoded for depth was performed on the selected PAM images (Fig. 5a–b). These images show that high PAM contrast was achieved at 1–48 h post-injection. Compared to pre-injection, the measured PAM signal amplitudes enhanced 10.4-fold from 1.25 ±0.06 (a.u.) for pre-injection to 0.12 ± 0.01 (a.u.) for post-injection at 1 h and reached peak at 48 h post-injection with the PA signal increased by up to 27.2-fold (PASignal = 3.28 ± 0.09 (a.u.)) (Fig. 5c). To examine the potential of photobleaching, 3D volumetric and MIP PAM images were acquired three times at the same scanning area on the same rabbit (Fig. 5d–f). The results show that PAM contrast did not change significantly. Compared to the first acquisition, the PAM signal amplitudes fluctuated about 1.4–5.6% for the second and the third scanning (PASignal = 2.23 ± 0.13, 2.26 ± 0.06, and 2.14 ± 0.12 (a.u.) for the first, the second, and the third acquisitions, respectively), confirming the photostability (Fig. 5g).

The location of newly developed CNV was further quantified using OCT imaging as an independent method. The OCT images were also acquired longitudinally over a period of 14 days. Figure 6 shows the cross-sectional B-scan OCT images acquired along the CNV. These OCT images show different layers of the retina. Before the injection, the position of CNV was hardly distinguishable on the OCT image due to strong scattering of the surrounding vasculature. After injection, CNV was clearly distinguished with high contrast. The OCT

signal intensity at CNV regions of interest (ROI) and the adjacent ROI was measured before and after the injection (Fig. S5). The OCT signal increase was quantified as a function of the injection time (Fig. 6q). The GNR-RGD binding to CNV produced strong OCT signal and led to a 171.4% OCT signal enhancement at 48 h post-injection when compared to the adjacent tissue and pre-injection.

To assess reproducibility of GNR-RGD targeting CNV, another CNV model created by subretinal injection of VEGF-165 was validated. CNV developed at day 7 post-injection of VEGF- 165, and 400 μL of GNR-RGD at concentration of 2.5 mg/mL was intravenously injected into the rabbit. Multimodal PAM and OCT and color fundus photography, and ICGA were acquired before and up to 28 days post-injection. Figure 7a shows color fundus photography and Figs. 7b–d show the ICGA images. CNV was observed on late phase FA and ICGA by leakage (white arrows). Longitudinal MIP PAM images were acquired at 578 and 700 nm and displayed in Fig. 7e–g. The PAM images acquired using the excitation wavelength of 700 nm at 24 h post-injection demonstrated significant increase of PAM contrast in the CNV compared with pre-injection. The PAM signal at the selected ROI on PAM acquired at each time point was quantified and plotted in Fig. 7h. The results show that the GNR-RGD generated 11.7-fold increase in PAM signal at 1 h post-injection compared to pre-injection. The peak PAM signal occurred at 48 h post-injection and exhibited 20.4-fold PAM signal enhancement. To examine the targeting ability of GNR-RGD when compared to unconjugated GNR, a group of rabbits with CNV models injected with GNR at a concentration of 2.5 mg/mL (400 μL) were imaged with PAM at different time points (i.e., 2, 24, and 48 h). There was minimal PA signal observed on the PAM images acquired under laser illumination at a wavelength of 700 nm (Fig. S6).

OCT images were also obtained before injection and followed up to 28 days post-injection (Figure 8a). Figure 8b show a magnification of the selected area (red rectangle) displayed in Figure 8a. The position and margin of CNV were clearly visualized (red arrows). The OCT signal around CNV was calculated at different time points (Fig. 8c). At 72 h post-injection, the OCT signal enhanced 161.3% in comparison with pre-injection (OCTSignal = 217.62 ± 1.99 (a.u.) at day 3 post- injection *vs* 134.94 ± 10.89 (a.u.) for pre-injection). With unconjugated GNR, the OCT signal was not increased significantly, and the location of CNV was not clearly observed when compared to that of before the injection (Fig. S7). To validate the capability of multimodality PAM and OCT imaging system for improved diagnosis of CNV, a fusion *en-face* volumetric OCT and PAM images obtained at 700 nm was co-registered on the same orthogonal imaging plane as presented in Figure 9. This image shows clearly scattering features of CNV (pseudo yellow color)

Histology, biodistribution, and biosafety evaluation:

To assess *in vivo* potential cytotoxicity of the GNR-RGD, body weights of the rabbits after administration of GNR-RGD were measured along with liver function tests (LFTs), kidney function tests, TUNEL assay, and histology. Hematoxylin and eosin (H&E) staining, and TUNEL assay were implemented to assess pathogenesis of CNV as well as to evaluate the potential apoptosis of GNR-RGD to eye tissue and organs post-administration (Fig. 10a–h). CNV was clearly visualized in the H&E images (Fig. 10a–c). No abnormal cellular

morphology or structural degradation of retinal cells was observed in these images. The developed CNV was clearly observed in the H&E images (Fig. 10b–c). No evidence of apoptotic cells was observed on TUNEL stained images (Fig. 10d–f). Note that the cell nuclei were stained with blue fluorescence using DAPI and the apoptotic cells were stained with FITC fluorescent dye (green fluorescent color). These results imply that no systemic toxicity was caused by GNR-RGD. Similarly, there is no evidence of tissue destruction or TUNEL-positive cells observed on H&E images (Fig. 9g) and TUNEL staining (Fig. 10h). To further examine any potential effect of GNR-RGD to the animal, body weight was measured, and LFTs were employed. As shown in Table 1, all rabbit liver and kidney function such as alanine amino transferase (ALT), alkaline phosphatase (ALP), and blood urea nitrogen (BUN) are within normal range, indicating that GNR-RGD did not induce any severe liver or kidney toxicity to the animals. The body weight was also increased appropriately over a period of 28 days, further confirming that GNR-RGD is safe (Fig. 10i). Fig 10j exhibits a graph of the biodistribution of GNR-RGD measured from different organs. The administrated nanoparticles (GNR and GNR-RGD) primarily accumulated in spleen and liver after 28 days. In contrast, minimal nanoparticles were detected in heart, lung, kidney and blood. This result is consistent with a reported by Niidome *et al.* and Li *et al*[50,51]

This work demonstrates targeted GNRs as a molecular contrast agent for multimodal PAM and OCT to selectively distinguish CNV in large animal eyes. By conjugation with molecular targeting peptides, GNR-RGD targeted CNV and produced excellent dual PAM and OCT signals in the NIR optical range, enabling for enhanced identification of CNV from the surrounding normal microvasculature in the retina. The experimental results demonstrated that the GNR-RGD contrast agent has excellent biocompatibility and photostability. No significant toxicity was observed *in vitro* or *in vivo*. The strong optical absorption coefficient of GNRs in the NIR spectrum could significantly benefit PAM imaging of the targeted molecular markers, because in this spectrum, such as 700 nm, the optical absorption from native chromophores such as hemoglobin are relatively lower. When working in this spectrum, the GNR-RGD targeting $\alpha v\beta 3$ integrin offer an opportunity to boost the sensitivity of PAM to distinguish CNV from normal microvasculature. GNRs have been widely used as photoacoustic and OCT contrast agents for improved visualization of several biological tissues such as neovascularization in tumors and labeling and imaging of stem cells[37,45,52,53]. A study reported by Lapierre-Landry *et al.* and Gorden *et al.* have used GNRs as contrast agent to enhance visualization of laser-induced choroidal neovascularization lesions[54,55]. To date, no study has used GNRs as a contrast agent for PAM imaging to enhance the visualization of abnormal neovascularization in the eye. The current study demonstrated that targeted GNR-RGD could serve as a molecular contrast agent to enhance both PAM and OCT signals. With the administration of GNR-RGD, PAM and OCT signals were significantly increased by up to 27.2-fold for PAM and by up to 171.4% for OCT due to strong absorption and scattering properties of the GNRs. In addition, the PAM images were obtained by using two different wavelengths of 578 and 700 nm, allowing for selective distinguishing of CNV from background normal microvasculature. This is important in clinical applications for diagnosis and monitoring of CNV pathogenesis. In addition, the use of GNRs demonstrated minimal toxicity to cells or *in vivo*. This is consistent with previous studies reported by Chen *et al.*[53]. These studies demonstrated that

GNRs induced very minimal toxicity to cells or animals. Under laser illumination, GNRs demonstrated great photostability without significant redshift in the absorption spectrum (Fig. 1f) and generated stable PAM signal amplitudes at multiple scanning times at the same location (Fig. 2c). Another benefit is that GNR-RGD can specifically label CNV for up to 5 days due to not only the selectively targeting of RGD to $\alpha_v\beta_3$ integrin overexpressed in CNV but also the enhanced permeability and retention (EPR) effects of CNV. The morphometric characteristics of CNV make the functionalized GNRs to be an ideal candidate as a dual-modality contrast agent for studying CNV by both PAM and OCT.

CNV is currently monitored using FA, ICGA, OCT, and OCTA. FA and ICGA can provide the location of CNV via leakage after injection of fluorescent chromophores[56–58]. However, these imaging techniques cannot provide depth information of the vascular network. In addition, the margin of CNV could not be identified clearly due to the extravasation of the fluorescent compound over time post-injection. OCT and OCTA could provide more information of the vasculature in both 2D and 3D with great image contrast[56,59,60]. A weakness of OCTA is that it is based on the motion of blood flow, and thus it has limited sensitivity to detect the slow flow of red blood cells within the neoangiogenic choroidal capillaries, resulting in difficulties to detect the precise location of CNV. Comparing these imaging systems, PAM offers several advantages such as greater penetration depth and 3D imaging capability. In addition, PAM is based on the optical absorption rather than optical scattering which is intrinsically strong in tissues. By using PAM powered by molecular targeting contrast agents, the target tissues can be selectively distinguished by performing multi-wavelength imaging and later spectral unmixing.

Before clinical translation, several items need to be addressed. First, the acquisition speed is important and should be further improved. High acquisition speed will help to avoid motion artifacts, enabling improved image quality. Currently, it took about 65 s to obtain a 3D volumetric image with the field of view (FOV) of 5×5 mm^2 with a resolution of 256×256 pixels. This acquisition speed is limited by the OPO repetition rate of 1 kHz. A study reported by Song and Liu *et al.* showed that their system could achieve an image with FOV of 2×3 mm^2 within 2.7 s by using a single wavelength laser with the repetition rate of 30 kHz. Therefore, it is possible to improve the scanning time by switching to commercially available laser systems with a higher pulse repetition rates[16,61,62]. Second, the PAM and OCT imaging in this study were performed sequentially, and the PAM and OCT images were not obtained at the same time. This further prolonged the image acquisition time. PAM and OCT imaging can be performed simultaneously, as recently reported by our group[23]. Further long-term safety studies including in humans would need to be conducted. In addition, comparison of this imaging technology with currently available clinical methods (such as FA and OCTA) would need to be performed along with understanding the timetable of injection and monitoring post-injection.

Conclusions

In summary, this study demonstrates multimodal, high resolution PAM and OCT molecular imaging of CNV enhanced by plasmonic GNR-RGD with strong optical absorption and scattering in the NIR spectrum. This study investigated the capability of such a multimodal

molecular imaging technique for visualization of CNV in living, large animal eyes. The experimental results demonstrated that the PAM signal amplitudes and OCT signal intensities were enhanced by GNRs by up to 27.2-fold and 171.4%, respectively, when compared to those of pre- injection. In addition, the margin and location of CNV were clearly visualized and distinguished from the surrounding normal microvasculature with high contrast and high resolution. This imaging technique can provide important information of CNV pathogenesis through precise identification of CNV. The functionalized GNR-RGD demonstrated great biocompatibility and excellent photostability both *in vitro* and *in vivo*. These results illustrated that targeting GNR-RGD offer an excellent dual PAM and OCT contrast agent for improving visualization of neovascular diseases in ophthalmology.

Methods/Experimental

Physical and optical characterization of targeting GNR contrast agent:

Functionalized GNR with Arginine–Glycine–Aspartic (RGD) peptides (GNR-RGD) nanoparticles were purchased from Nanopartz (Nanopartz Inc., USA) and utilized as multimodal PAM and OCT image contrast agent. Physical and optical properties of nanoparticles were analyzed. Ultraviolet- visible (UV-Vis) spectroscopy (UV-3600, Shimadzu Corp., Japan) was used to assess the optical absorption spectra of GNR. The absorption spectrum was measured from the wavelength of 400 to 1000 nm. Transmission electron microscopy (TEM) was performed to visualize the morphology of GNR (JEOL 2010F, Japan) and to evaluate the stability of GNR-RGD samples kept in room temperature at different times (i.e., 1 week, 2 weeks, and 4 weeks). The particle size distribution of GNR was quantified by measuring 250 nanoparticles on the TEM image using ImageJ (National Institute of the Health, Bethesda, MD, USA). Dynamic light scattering (DLS) was analyzed to determine hydrodynamic diameter of the GNR and zeta potential value was characterized using an electrophoretic light scattering spectrophotometer (Nano-ZS90 Zetasizer, Malvern Instrument, Westborough, MA) at a fixed angle of 90° and room temperature. The ratio between gold nanoparticles and organic compounds material was determined by thermogravimetric analysis (TGA) on desiccated samples. The TGA analysis was employing on a TGA7 Pyris 1 instruments with two mass flow controllers (Perkin Elmer, Waltham, Massachusetts, USA). The samples were placed in an aluminum holder and heated from room temperature to 550 °C under the nitrogen (60 mL/min), then switched to air and heated up to 770 °C a with an increase in temperature of 10 °C/min. The Curie point of Ni wire was utilized to calibrate the TGA. The infrared spectra of the chemical functional groups such as PEG 2k-SH, RGD, bare GNR, and GNR-RGD were performed using Fourier transformed infrared spectroscopy (FTIR) spectrometer. The FTIR analysis was performed on a PerkinElmer spectrum 100 (PerkinElmer Inc., Waltham, MA) equipped with an attenuated total reflection diamond.

Biocompatibility analysis of GNR-RGD: The potential cytotoxicity of GNR-RGD was examined on three different cells lines: HeLa, bovine retinal endothelial cells (BRECs), and brain endothelial cells (b.End 3) cells. HeLa cells were purchased from ATCC (ATCC, Manassas, Virginia, USA). BRECs and b.End3 were provided by the generous assistance of Dr. David Antonetti. The HeLa and b.End3 cells were seeded in complete DMEM

supplemented with 10% fetal bovine serum (FBS) and antibiotic (1%, 1.0 g mL^{-1}). For culturing BREC cells, the tissue culture dishes were first coated with fibronectin at a concentration of 1 μg/mL for 1–4 hours at room temperature. Then, the cells were cultured in MCDB-131supplemented with 10% FBS, 1.18 g sodium bicarbonate, 20 ng/mL EGF, 200 mg EndoGRO, 90 mg heparin, 1 mL tylosin, and 10 mL antibiotics/antimycotics. The cells were incubated at 37°C in humidified atmosphere with 5% CO2 and 95% air. When the cells confluence reached 70–90%, they were harvested by adding 1 mL of 0.25% trypsin-EDTA solution and incubated for 3 min. The trypsinized cells were centrifuged at 500 rpm for 5 min.

To evaluate the viability of cells after treatment with GNR-RGD, MTT assay was performed. The cells were cultured in 96-wells plates for 24 h at a density of 2×10^4 cells/well. Then, fresh medium containing GNR at different concentrations (*i.e.*, 12.5, 25, 50, 100, 200, 400, and 500 μg/mL) was added into the cells and incubated for 24 and 48 h. Then, 100 μL MTT solution at a concentration of 1 mg/mL in medium were added into each well and incubated for 4 h. Finally, 100 μL of DMSO were added into each well and maintained for 20 min. The cell viability was analyzed by measuring optical density (OD) at wavelength of 570 nm using an ELISA micro-plate reader (SpectraMax, 340, Molecular Device, Sunnyvale, CA, USA). The cells were incubated in standard culture medium as the control group. The cell viability was calculated by the formula:

$$\text{Survival rate } (\%) = 100 \times (OD_{\text{Treated}} / OD_{\text{Control}}) \quad (1)$$

where ODTreated and ODControl are optical density of treated and control, respectively.

To further quantify any chance of GNR-RGD induced apoptosis, flow cytometry analysis was implemented using an Annexin-V FITC Apoptosis Detection Kit. The cells were cultured in 30 mm tissue culture dishes for 24 h. Then, 20 μL of GNR-RGD at concentration of 5 mg/mL was added into the cells and incubated for 24 and 48 h. The cells were trypsinized, harvested, centrifuged, and re-suspended in 500 μL 1× buffer binding. Then, 5μL (10 μg/mL) of Annexin-V FITC and 5μL (10 μg/mL) of propidium iodide solution were added into the cells and maintained in a dark place for 15 min. Afterwards, the suspended cells were transferred to a 5 mL glass tube containing 1 mL cold PBD for flow cytometer analysis. Note that the cells unstained with PI and FITC or stained with PI only or FITC only were used a negative control.

Cellular uptake: To examine the successful targeting of GNR-RGD, the distribution of nanoparticles inside the cells was analyzed using confocal laser scanning microscopy analysis and custom molecular photoacoustic microscopy (PAM) imaging. The cells were seeded in 35 mm μ- plates with cover glass at the bottom at density of 2×10^5 cells/well and incubated at 37 °C and 5% CO2 for 24 h. Then, the cells were treated with ICG conjugated to GNR-RGD at a final concentration of 50, 100 and 200 μg/mL and incubated for 24 h. Cells not treated with GNR and treated with GNRs without conjugation to RGD were used as control. The cells were stained with DAPI, PI, and FITC fluorescent dye. A mixed solution of 500 μL 1X binding buffer, 5 μL of PI, and 5 μL of FITC was added to the cells

and incubated for 15 min. Then, the cells were fixed with 2.5 % of formaldehyde for 30 min. Finally, the cells were stained with DAPI (300 μL,10 μg/mL) for 20 min. The cells were washed 2 times with PBS and imaged with the SP5 confocal laser scanning microscope and PAM imaging. The internalized GNRs containing ICG molecules inside the cells were excited at the wavelength of 640nm (λex = 640 nm), and the emission band was detected in the range of 810–860 nm.

***In vitro* PAM and OCT characterization of GNR-RGD:** To assess the potential application of GNR-RGD as a dual PAM and OCT contrast agent, tissue mimicking phantoms were prepared and imaged using a custom PAM and OCT imaging system. For PAM imaging, a group of silicone tubes were prepared and filled with nanoparticles at various concentrations, ranging from 0–0.08 mg/mL. These samples were placed on cover glass and immersed in a degassed water tank. Then, the samples were imaged with PAM at an excitation wavelength of 700 nm and laser energy of ~40 nJ. Regions of interest (ROI) analysis was implemented to quantify the PA signal amplitudes. For OCT imaging, a group of six capillary glass tubes were poured with nanoparticles at different concentrations (*i.e.*, 0 (saline), 0.005, 0.01, 0.02, 0.04, and 0.08 mg/mL). The samples were placed on phantom mold and imaged with the OCT system.

Choroidal neovascularization (CNV) model in living rabbits: CNV models were created in two groups of rabbits. A group of three rabbits received laser-induced retinal vein occlusion (RVO) and a group of three rabbits received subretinal injection of human vascular endothelial growth factor (VEGF-165). All animal experiments were conducted in accordance with the guidance of the Association for Research in Vision and Ophthalmology (ARVO) Statement on the Use of Laboratory Animals in Ophthalmic and Vision Research. The experiment protocols were approved by the University of Michigan's Institutional Animal Care and Use Committee (IACUC) (PRO00008566, PI: Y. Paulus). The rabbits were donated from the Center for Advanced Models and Translational Sciences and Therapeutics (CAMTraST) at the University of Michigan Medical School.

Laser-induced RVO models were employed using the Vitra 532nm Photocoagulator (Quantel Medical, Cournon d'Auvergne, France) as described in our previous studies[24,26]. Briefly, a contact lens (Volk H-R Wide Field, laser spot 2x magnification, Volk Optical Inc, Mentor, OH, USA) filled with Gonak coupling gel (Akorn, Lake Forest, IL, USA) was mounted on the cornea of the rabbit eye. Rose Bengal at concentration of 50 mg/kg was injected into the rabbit intravenously via the marginal ear vein. After waiting 5 seconds, laser illumination was commenced. Each retinal vein was irradiated with laser at a power of 150 mW with pulse duration of 0.5 s and laser spot size of 75 μm. Twenty shots of the laser were administered at the same position until vessels occlusion was observed. To prevent blood vessel reperfusion, 20 additional shots of laser at a power of 300 mW was further applied.

Subretinal injection of human VEGF-165 was employed by using a mixed solution of VEGF-165 (Shenandoah Biotechnology, Warwick, USA) and Matrigel basement membrane matrix (Corning, NY, USA). A stock solution of VEGF-165 at concentration of 100 μg/mL in 1% bovine serum albumin was prepared. Then, 20 μL of Matrigel was mixed with 750

ng VEGF. The suspended solution was injected into the subretinal space in the retina as described previously[63].

Prior to each animal experiment, the animals were anesthetized by intramuscular injection of ketamine (40 mg/kg) and xylazine (5 mg/kg). To maintain adequate anesthesia, about 1/3 dose of ketamine solution was injected every 35–45 min. One drop of tropicamide 1% ophthalmic and phenylephrine hydrochloride 2.5% ophthalmic were added into the rabbit's eyes to dilate their pupils. Topical local anesthesia was carried out by applying a drop of proparacaine hydrochloride 0.5% ophthalmic solution. The rabbit's body was placed on circulation heat blanket covered with an underpad (TP-700, Stryker Corporation, Kalamazoo, MI) to prevent a drop of body temperature during the experimentation. The animal vitals such as mucous membrane color, body temperature, heart rate, and respiratory rate were monitored and documented every 15 min.

Custom multimodal, high resolution PAM and OCT imaging platform: A custom multimodal, high resolution PAM and OCT imaging device (Fig. S1) was developed as described in our previous studies[13,14]. Briefly, a diode pumped Q-switched Nd:YAG laser and OPO system (NT- 242, Ekspla, Vilnius, Lithuania) was used to generate tunable nanosecond pulsed laser light (3~5 ns) with a pulse repetition rate of 1 kHz. The excitation wavelength can be adjusted from 405 to 2600 nm using a user-guidance controller. The laser light was filtered, collimated, and delivered to the rabbit eye through an optical system consisting of a scan lens (focal length 36 mm) and an ophthalmic lens (OL, focal length 10 mm). The collimated laser light has a circular-shaped pattern with an estimated spot size of ~2 mm at the cornea. The laser light as focused on the fundus by the rabbit eye optics with an approximate spot size of 20 μm. Two different excitation wavelengths of 578 and 700 nm were used to induce photoacoustic signals. The laser-induced photoacoustic signals were detected by a single element needle-shaped transducer with center frequency of 27 MHz (Optosonic Inc., Arcadia, CA, USA). The acoustic signal was amplified using a low-noise amplifier (gain 57 dB, AU-1647, L3 Narda-MITEQ, NY) and recorded by a 200 MHz digitizer (PX1500–4, Signatec Inc., Newport Beach, CA). By raster scanning along x- and y-axes using an optical-scanning galvanometer, three-dimensional photoacoustic data was achieved within 65 s with a resolution of 256 × 256 pixels. At the focal plane of the scan lens, the resolution was estimated to be 4.1 for lateral resolution and 37.0 μm for axial resolution using full-width at half- maximum (FWHM) analysis. The laser energy was approximately ~80 nJ which is about 50% below the American National Standards Institute (ANSI) safety limit.

Spectral domain optical coherence tomography (OCT) was developed from a Ganymede-II-HR OCT platform (Thorlabs, Newton, NJ). To integrate the modalities and apply them for large animal eyes, two additional components consisting of a scan lens and dispersion compensation glass were added to the system (Fig. S1)[13]. To induce coherence signal, two super luminescent diodes with center wavelength of 846 nm and 932nm were utilized to excite the samples. These excitation lights were coaxially aligned with the laser light from OPO to achieve multimodal imaging. The lateral and axial resolutions are 3.8 μm and 4.0 μm, respectively. Each B-scan OCT images were acquired within 0.103 seconds with a resolution of 512 × 1024 A-lines and acquisition speed of 36 kHz.

***In vivo* choroidal neovascularization monitoring:** The developed choroidal neovascularization (CNV) was monitored using multimodal imaging, including color fundus photography, fluorescein angiography (FA), indocyanine green angiography (ICGA), and custom photoacoustic microscopy and optical coherence tomography (OCT) system.

Color fundus photography:

50-degree color fundus photography (Topcon 50EX, Topcon Corporation, Tokyo, Japan) was used to monitor retinal and choroidal vessels before and after generating CNV. For the RVO model, color fundus images were used to determine the selected retinal veins as well as the target position for laser illumination. After generating the RVO model, fundus color photography used to evaluate the perfusion and non-perfusion of the occluded vessels. For the subretinal injection model, color fundus photography was used to evaluate the success of the injection. Color fundus images were acquired at different positions: the optic nerve, the superior retina above the optic disc, the inferior retina below the optic disc, the temporal medullary ray, and the nasal medullary ray.

Fluorescein angiography (FA) and indocyanine green angiography (ICGA):

After taking the fundus images, FA and ICGA were sequentially employed by using the same fundus photography system (Topcon 50EX). To switch to fluorescent channels, internal excitation and emission filters were changed. Fluorescein angiography was obtained by intravenous injection of 0.2 mL fluorescein sodium at a concentration of 10% fluorescein (Akorn, Lake Forest, IL, USA). ICGA was obtained by intravenous injection of 2.5 mg/mL of ICG fluorescent solution (Akorn, Lake Forest, IL, USA). Late phase FA and ICGA images were obtained at every minute for a period of at least 20 minutes.

In vivo PAM and OCT monitoring:

PAM and OCT images were acquired before and after intravenous injection of targeting GNR-RGD (0.4 mL; 2.5 mg/mL) at 2 h, 4 h, 8 h, 24 h, 48 h, 72 h, and days 5, 7, 9, 11, and 14 using the custom PAM and OCT imaging system. To acquire PAM and OCT images, the head and body of the anesthetized rabbit were placed on two different stabilization linear stages to avoid motion artifacts. The fundus of the rabbits' retina was monitored in real-time using a CCD camera integrated on the OCT system to select the target vessels and scanning areas. Cross-sectional B-scan OCT image were acquired. OCT images were acquired at the position of CNV and the adjacent areas. Then, the system was switched to the PAM module to acquire PAM images. The PAM images were acquired using the optical excitation wavelength of 578 nm and 700 nm. The laser energy was approximately ~80 nJ. The resolution of the raster- scanning is 256 × 256 pixels. Optical scanning methods were used to acquire three-dimensional volumetric PAM data. Three-dimensional volumetric visualization was rendered using Amira software (Amira 6.0, FEI, Thermo Fisher Scientific, MA, USA).

Histopathology, TUNEL assay and biodistribution of GNR in tissues:

Biosafety was evaluated on all treated animals using histopathological analysis, TUNEL assay, liver function test (LFTs), kidney function tests (KFTs), and H&E staining. All

treated animals including the control group were euthanized at day 28 post-injection of functionalized GNR-RGD. Prior to euthanizing the animals, blood serum was collected for LFTs and KFTs. The animals were euthanized by intravenous injection of euthanasia solution (0.22 mg/kg) into the rabbits via the marginal ear vein (Beuthanasia-D Special, Intervet Inc., Madison, NJ, USA). The eye tissues and various organs were isolated from the euthanized rabbits. Eye tissues were immersed in Davidson's fixative solution (Electron Microscope Sciences, PA, USA) and kept at room temperature for 24 h. Organs were fixed with 10% neutral buffered formalin (VWR, Radnor, PA, USA). The fixed samples were sectioned into 4–6 mm samples and embedded in paraffin. These samples were then sectioned into 6 μm thick sections using a Leica autostainer XL (Leica Biosystems, Nussloch, Germany). Three specimens were placed on each slide. These slides were stained with hematoxylin and eosin (H&E) for histopathological examination. For apoptosis detection, the sectioned samples were implemented following TUNEL *in situ* Cell Death Detection Kit protocol (Sigma-Aldrich, USA). IHC analysis was performed by staining the sectioned slide with SMA. The stained slides were observed using DM6000 microscope. H&E and IHC photography were obtained using the BF450C camera. TUNEL fluorescence images were achieved using the FF363x camera (for TUNEL) (DM600, Leica Biosystems, Nussloch, Germany). The biodistribution of GNR and GNR-RGD was measured in different tissues including lung, liver, heart, spleen, kidney and blood using ICP MS analysis. The tissues were isolated from the euthanized rabbits. These tissues were washed with PBS to remove blood and weighted accurately (~0.2 g). Then, the samples were dissolved in a 1 mL concentrated 67% nitric acid for 3 minutes at a temperature of 100 °C. Afterwards, 3 mL hydrochloric acid was added into the boiled solution and heated at 180 °C until the mixed solution reached 1 mL. The solutions were diluted in 5 mL deionized water and filtered with 0.22 μL cellulose nitrate syringe filter (Merc Millipore Ltd., Co. Cork, Ireland). The amount of GNR was measured using inductively coupled plasma mass spectrometer (ICP-MS) (iCAP™ RQ ICP-MS, Thermo Fisher Scientific, Bremen, Germany).

Supplementary Material

Refer to Web version on PubMed Central for supplementary material.

Acknowledgments

This work was supported by the National Eye Institute (grant number: 1K08EY027458 (YMP)) and Fight for Sight-International Retinal Research Foundation (grant number: FFSGIA16002 (YMP). This work was also assisted by unrestricted departmental support from Research to Prevent Blindness and the University of Michigan Department of Ophthalmology and Visual Sciences. A part of this research utilized the Core Center for Vision Research funded by the National Eye Institute (grant number: P30 EY007003). The authors thank Dr. Yuqing Chen and the Center for Advanced Models and Translational Sciences and Therapeutics (CAMTraST) at the University of Michigan Medical School for the generous donation of New Zealand rabbits, Dr. David Antonetti for the generous donation of BREC and b.End3 cells, Dr. Thomas David for assistance with immunohistochemistry, Dr. Wei Qian for assistance with DLS and FT-IR measurements, and Dr. Stephen Lentz, Dr. Qitao Zhang, and Dr. Xuwen Liu for helping with the confocal microscopy.

References

1. Wong WL; Su X; Li X; Cheung CMG; Klein R; Cheng C-Y;Wong TY Global Prevalence of Age-Related Macular Degeneration and Disease Burden Projection for 2020 and 2040: A Systematic Review and Meta-Analysis. Lancet Glob Health 2014, 2, e106–e116. [PubMed: 25104651]

2. Jager RD; Mieler WF;Miller JW Age-Related Macular Degeneration. New Eng J Med 2008, 358, 2606–2617. [PubMed: 18550876]
3. Ambati J;Fowler BJ Mechanisms of Age-Related Macular Degeneration. Neuron 2012, 75, 26–39. [PubMed: 22794258]
4. Grossniklaus HE;Green WR Choroidal Neovascularization. Am. J. Ophthalmol. 2004, 137, 496–503. [PubMed: 15013874]
5. Coscas GJ; Lupidi M; Coscas F; Cagini C;Souied EH Optical Coherence Tomography Angiography Versus Traditional Multimodal Imaging in Assessing the Activity of Exudative Age-Related Macular Degeneration: A New Diagnostic Challenge. Retina 2015, 35, 2219–2228. [PubMed: 26398697]
6. Rickman CB; Farsiu S; Toth CA;Klingeborn M. Dry Age-Related Macular Degeneration: Mechanisms, Therapeutic Targets, and Imaging. Invest Ophthal Vis Sci 2013, 54, ORSF68-ORSF80.
7. Dysli C; Wolf S; Berezin MY; Sauer L; Hammer M;Zinkernagel MS Fluorescence Lifetime Imaging Ophthalmoscopy. Prog. Retin. Eye Res 2017, 60, 120–143. [PubMed: 28673870]
8. Smailhodzic D; Fleckenstein M; Theelen T; Boon CJ; van Huet RA; van de Ven JP; Den Hollander AI; Schmitz-Valckenberg S; Hoyng CB;Weber BH Central Areolar Choroidal Dystrophy (Cacd) and Age-Related Macular Degeneration (Amd): Differentiating Characteristics in Multimodal Imaging. Invest Ophthal Vis Sci 2011, 52, 8908–8918. [PubMed: 22003107]
9. Sauer L; Komanski CB; Vitale AS; Hansen ED;Bernstein PS Fluorescence Lifetime Imaging Ophthalmoscopy (Flio) in Eyes with Pigment Epithelial Detachments Due to Age-Related Macular Degeneration. Invest Ophthal Vis Sci 2019, 60, 3054–3063. [PubMed: 31348823]
10. Wang LV Multiscale Photoacoustic Microscopy and Computed Tomography. Nat. Photonics 2009, 3, 503–509. [PubMed: 20161535]
11. Beard P. Biomedical Photoacoustic Imaging. Interface focus 2011, 1, 602–631. [PubMed: 22866233]
12. Vo-Dinh T. Biomedical Photonics Handbook: Biomedical Diagnostics. (CRC press, 2014).
13. Tian C; Zhang W; Mordovanakis A; Wang X;Paulus YM Noninvasive Chorioretinal Imaging in Living Rabbits Using Integrated Photoacoustic Microscopy and Optical Coherence Tomography. Opt. Express 2017, 25, 15947–15955. [PubMed: 28789105]
14. Tian C; Zhang W; Nguyen VP; Wang X;Paulus YM Novel Photoacoustic Microscopy and Optical Coherence Tomography Dual-Modality Chorioretinal Imaging in Living Rabbit Eyes. J. Vis. Exp. JOVE 2018, e57135.
15. Song W; Wei Q; Jiao S;Zhang HF Integrated Photoacoustic Ophthalmoscopy and Spectral-Domain Optical Coherence Tomography. J. Vis. Exp. JOVE 2013, 4390. [PubMed: 23354081]
16. Jiao S; Jiang M; Hu J; Fawzi A; Zhou Q; Shung KK; Puliafito CA;Zhang HF Photoacoustic Ophthalmoscopy for in Vivo Retinal Imaging. Opt. Express 2010, 18, 3967–3972. [PubMed: 20389409]
17. Nguyen VP;Paulus YM Photoacoustic Ophthalmoscopy: Principle, Application, and Future Directions. J. Imaging 2018, 4, 149. [PubMed: 31681819]
18. Dai C; Li L; Liu W; Wang F;Zhou C. in Photons Plus Ultrasound: Imaging and Sensing 2018. 1049469 (International Society for Optics and Photonics).
19. Jeon S; Song HB; Kim J; Lee BJ; Managuli R; Kim JH; Kim JH;Kim C. In Vivo Photoacoustic Imaging of Anterior Ocular Vasculature: A Random Sample Consensus Approach. Sci. Rep. 2017, 7, 1–9. [PubMed: 28127051]
20. Nguyen VP; Li Y; Aaberg M; Zhang W; Wang X;Paulus YM In Vivo 3d Imaging of Retinal Neovascularization Using Multimodal Photoacoustic Microscopy and Optical Coherence Tomography Imaging. J. Imagin 2018, 4, 150.
21. Zhang W; Li Y; Nguyen VP; Huang Z; Liu Z; Wang X;Paulus YM High- Resolution, in Vivo Multimodal Photoacoustic Microscopy, Optical Coherence Tomography, and Fluorescence Microscopy Imaging of Rabbit Retinal Neovascularization. Light Sci. Appl. 2018, 7, 1–12. [PubMed: 30839587]

22. Nguyen VP; Li Y; Henry J; Zhang W; Wang X;Paulus YM High Resolution Multimodal Photoacoustic Microscopy and Optical Coherence Tomography Visualization of Choroidal Vascular Occlusion. Int. J. Mol. Sci. 2020, 21, 6508.
23. Zhang W; Li Y; Yu Y; Derouin K; Qin Y; Nguyen VP; Xia X; Wang X;Paulus YM Simultaneous Photoacoustic Microscopy, Spectral-Domain Optical Coherence Tomography, and Fluorescein Microscopy Multi-Modality Retinal Imaging. Photoacoustics 2020, 100194. [PubMed: 32566480]
24. Nguyen VP; Li Y; Zhang W; Wang X;Paulus YM Multi-Wavelength, En-Face Photoacoustic Microscopy and Optical Coherence Tomography Imaging for Early and Selective Detection of Laser Induced Retinal Vein Occlusion. Biomed. Opt. Express 2018, 9, 5915–5938. [PubMed: 31065403]
25. Nguyen V-P; Li Y; Henry J; Zhang W; Aaberg M; Jones S; Qian T; Wang X;Paulus YM Plasmonic Gold Nanostar-Enhanced Multimodal Photoacoustic Microscopy and Optical Coherence Tomography Molecular Imaging to Evaluate Choroidal Neovascularization. ACS Sens 2020, 5, 3070–3081. [PubMed: 32921042]
26. Nguyen VP; Li Y; Zhang W; Wang X;Paulus YM High-Resolution Multimodal Photoacoustic Microscopy and Optical Coherence Tomography Image-Guided Laser Induced Branch Retinal Vein Occlusion in Living Rabbits. Sci. Rep. 2019, 9, 1–14. [PubMed: 30626917]
27. Hughes A. A Schematic Eye for the Rabbit. Vis. Res. 1972, 12, 123-IN126.
28. Nguyen VP; Folz J; Li Y; Henry J; Zhang W; Qian T; Wang X;Paulus YM Indocyanine Green-Enhanced Multimodal Photoacoustic Microscopy and Optical Coherence Tomography Molecular Imaging of Choroidal Neovascularization. J. Biophotonics 2021, e202000458.
29. Nguyen VP; Qian W; Li Y; Liu B; Aaberg M; Henry J; Zhang W; Wang X;Paulus YM Chain-Like Gold Nanoparticle Clusters for Multimodal Photoacoustic Microscopy and Optical Coherence Tomography Enhanced Molecular Imaging. Nat. Commun. 2021, 12, 1–14. [PubMed: 33397941]
30. Zhang W; Li Y; Nguyen VP; Huang Z; Liu Z; Wang X;Paulus YM High- Resolution, in Vivo Multimodal Photoacoustic Microscopy, Optical Coherence Tomography, and Fluorescence Microscopy Imaging of Rabbit Retinal Neovascularization. Light Sci. Appl. 2018, 7, 103. [PubMed: 30534372]
31. Nguyen VP; Li Y; Zhang W; Wang X;Paulus YM High-Resolution Multimodal Photoacoustic Microscopy and Optical Coherence Tomography Image-Guided Laser Induced Branch Retinal Vein Occlusion in Living Rabbits. Sci. Rep. 2019, 9, 10560. [PubMed: 31332266]
32. Nguyen VP; Li Y; Henry J; Rosen R; Aaberg M; Zhang W; Wang X;Paulus YM in Multimodal Biomedical Imaging XIV. 1087104 (International Society for Optics and Photonics).
33. Jathoul AP; Laufer J; Ogunlade O; Treeby B; Cox B; Zhang E; Johnson P; Pizzey AR; Philip B;Marafioti T. Deep in Vivo Photoacoustic Imaging of Mammalian Tissues Using a Tyrosinase-Based Genetic Reporter. Nat. Photonics 2015, 9, 239.
34. Pu K; Shuhendler AJ; Jokerst JV; Mei J; Gambhir SS; Bao Z;Rao J. Semiconducting Polymer Nanoparticles as Photoacoustic Molecular Imaging Probes in Living Mice. Nat. Nanotechnol. 2014, 9, 233. [PubMed: 24463363]
35. Zhang Y; Jeon M; Rich LJ; Hong H; Geng J; Zhang Y; Shi S; Barnhart TE; Alexandridis P;Huizinga JD Non-Invasive Multimodal Functional Imaging of the Intestine with Frozen Micellar Naphthalocyanines. Nat. Nanotechnol. 2014, 9, 631. [PubMed: 24997526]
36. Nguyen VP; Kim H; Kang M; Kwak M;Kang HW Application of Organic Ir788- Loaded Semi-Interpenetrating Network Dyes for Photoacoustic Imaging. Jpn J Appl Phys (2008) 2017, 56, 07JF12.
37. Liba O; SoRelle ED; Sen D;de La Zerda A. Contrast-Enhanced Optical Coherence Tomography with Picomolar Sensitivity for Functional in Vivo Imaging. Sci. Rep. 2016, 6, 1–12. [PubMed: 28442746]
38. Nguyen VP; Li Y; Qian W; Liu B; Tian C; Zhang W; Huang Z; Ponduri A; Tarnowski M;Wang X. Contrast Agent Enhanced Multimodal Photoacoustic Microscopy and Optical Coherence Tomography for Imaging of Rabbit Choroidal and Retinal Vessels in Vivo. Sci. Rep. 2019, 9, 1–17. [PubMed: 30626917]
39. Nguyen VP; Park S; Oh J;Wook Kang H. Biocompatible Astaxanthin as Novel Contrast Agent for Biomedical Imaging. J. Biophotonics 2016.

40. Mallidi S; Larson T; Tam J; Joshi PP; Karpiouk A; Sokolov K;Emelianov S. Multiwavelength Photoacoustic Imaging and Plasmon Resonance Coupling of Gold Nanoparticles for Selective Detection of Cancer. Nano Lett. 2009, 9, 2825–2831. [PubMed: 19572747]
41. Chen Y-S; Frey W; Kim S; Homan K; Kruizinga P; Sokolov K;Emelianov S. Enhanced Thermal Stability of Silica-Coated Gold Nanorods for Photoacoustic Imaging and Image-Guided Therapy. Opt Express 2010, 18, 8867–8878. [PubMed: 20588732]
42. Wang Y; Xie X; Wang X; Ku G; Gill KL; O'Neal DP; Stoica G;Wang LV Photoacoustic Tomography of a Nanoshell Contrast Agent in the in Vivo Rat Brain. Nano Lett. 2004, 4, 1689–1692.
43. Qian W; Murakami M; Ichikawa Y;Che Y. Highly Efficient and Controllable Pegylation of Gold Nanoparticles Prepared by Femtosecond Laser Ablation in Water. The J. Phys. Chem. C 2011, 115, 23293–23298.
44. Liba O; SoRelle ED; Sen D;de La Zerda A. Contrast-Enhanced Optical Coherence Tomography with Picomolar Sensitivity for Functional in Vivo Imaging. Sci. Rep. 2016, 6, 23337. [PubMed: 26987475]
45. Jokerst JV; Thangaraj M; Kempen PJ; Sinclair R;Gambhir SS Photoacoustic Imaging of Mesenchymal Stem Cells in Living Mice Via Silica-Coated Gold Nanorods. ACS nano 2012, 6, 5920–5930. [PubMed: 22681633]
46. Li Z; Huang P; Zhang X; Lin J; Yang S; Liu B; Gao F; Xi P; Ren Q;Cui D. Rgd-Conjugated Dendrimer-Modified Gold Nanorods for in Vivo Tumor Targeting and Photothermal Therapy. Mol. Pharm. 2010, 7, 94–104. [PubMed: 19891496]
47. Shen S; Tang H; Zhang X; Ren J; Pang Z; Wang D; Gao H; Qian Y; Jiang X;Yang W. Targeting Mesoporous Silica-Encapsulated Gold Nanorods for Chemo- Photothermal Therapy with near-Infrared Radiation. Biomaterials 2013, 34, 3150–3158. [PubMed: 23369218]
48. Lankveld DP; Rayavarapu RG; Krystek P; Oomen AG; Verharen HW; Van Leeuwen TG; De Jong WH;Manohar S. Blood Clearance and Tissue Distribution of Pegylated and Non-Pegylated Gold Nanorods after Intravenous Administration in Rats. Nanomedicine 2011, 6, 339–349. [PubMed: 21385136]
49. Akiyama Y; Mori T; Katayama Y;Niidome T. The Effects of Peg Grafting Level and Injection Dose on Gold Nanorod Biodistribution in the Tumor-Bearing Mice. J. Control. Release 2009, 139, 81–84. [PubMed: 19538994]
50. Niidome T; Yamagata M; Okamoto Y; Akiyama Y; Takahashi H; Kawano T; Katayama Y;Niidome Y. Peg-Modified Gold Nanorods with a Stealth Character for in Vivo Applications. J. Control. Release 2006, 114, 343–347. [PubMed: 16876898]
51. Li Z; Tang S; Wang B; Li Y; Huang H; Wang H; Li P; Li C; Chu PK;Yu X-F Metabolizable Small Gold Nanorods: Size-Dependent Cytotoxicity, Cell Uptake and in Vivo Biodistribution. ACS Biomater. Sci. Eng. 2016, 2, 789–797. [PubMed: 33440576]
52. Jokerst JV; Cole AJ; Van de Sompel D;Gambhir SS Gold Nanorods for Ovarian Cancer Detection with Photoacoustic Imaging and Resection Guidance Via Raman Imaging in Living Mice. ACS nano 2012, 6, 10366–10377. [PubMed: 23101432]
53. Chen Y-S; Zhao Y; Yoon SJ; Gambhir SS;Emelianov S. Miniature Gold Nanorods for Photoacoustic Molecular Imaging in the Second near-Infrared Optical Window. Nat. Nanotechnol. 2019, 14, 465–472. [PubMed: 30833692]
54. Lapierre-Landry M; Gordon AY; Penn JS;Skala MC In Vivo Photothermal Optical Coherence Tomography of Endogenous and Exogenous Contrast Agents in the Eye. Sci. Rep. 2017, 7, 1–9. [PubMed: 28127051]
55. Gordon AY; Lapierre-Landry M; Skala MC;Penn JS Photothermal Optical Coherence Tomography of Anti-Angiogenic Treatment in the Mouse Retina Using Gold Nanorods as Contrast Agents. Transl. Vis. Sci. Technol. 2019, 8, 18–18.
56. de Oliveira T; Isaac DLC; Garcia J. M. B. d. B.; Schelini MC;Avila MP. Oct Angiography Compared to Fluorescein Angiography, Indocyanine Green Angiography and Optical Coherence Tomography in the Detection of Choroidal Neovascularization in Pigment Epithelial Detachment. Acta Ophthalmol. 2019, 97, e1006–e1012. [PubMed: 31012539]

57. Feenstra DJ; Seleci M; Denk N; Fauser S; Drawnel FM;Jayagopal A. Indocyanine Green Molecular Angiography of Choroidal Neovascularization. Exp. Eye Res. 2019, 180, 122–128. [PubMed: 30582913]

58. Craandijk A;Van Beek C. Indocyanine Green Fluorescence Angiography of the Choroid. Br J Ophthalmol 1976, 60, 377–385. [PubMed: 952809]

59. Murakawa S; Maruko I; Kawano T; Hasegawa T;Iida T. Choroidal Neovascularization Imaging Using Multiple En Face Optical Coherence Tomography Angiography Image Averaging. Arch. Clin. Exp. Ophthalmol. 2019, 257, 1119–1125.

60. Querques G; Corvi F; Querques L; Souied EH;Bandello F. in Oct Angiography in Retinal and Macular Diseases Vol. 56 101–106 (Karger Publishers, 2016).

61. Liu T; Li H; Song W; Jiao S;Zhang HF Fundus Camera Guided Photoacoustic Ophthalmoscopy. Curr. Eye Res. 2013, 38, 1229–1234. [PubMed: 24131226]

62. Liu W;Zhang HF Photoacoustic Imaging of the Eye: A Mini Review. Photoacoustics 2016, 4, 112–123. [PubMed: 27761410]

63. Li Y; Zhang W; Nguyen VP; Rosen R; Wang X; Xia X;Paulus YM Real-Time Oct Guidance and Multimodal Imaging Monitoring of Subretinal Injection Induced Choroidal Neovascularization in Rabbit Eyes. Exp. Eye Res. 2019, 186, 107714. [PubMed: 31288022]

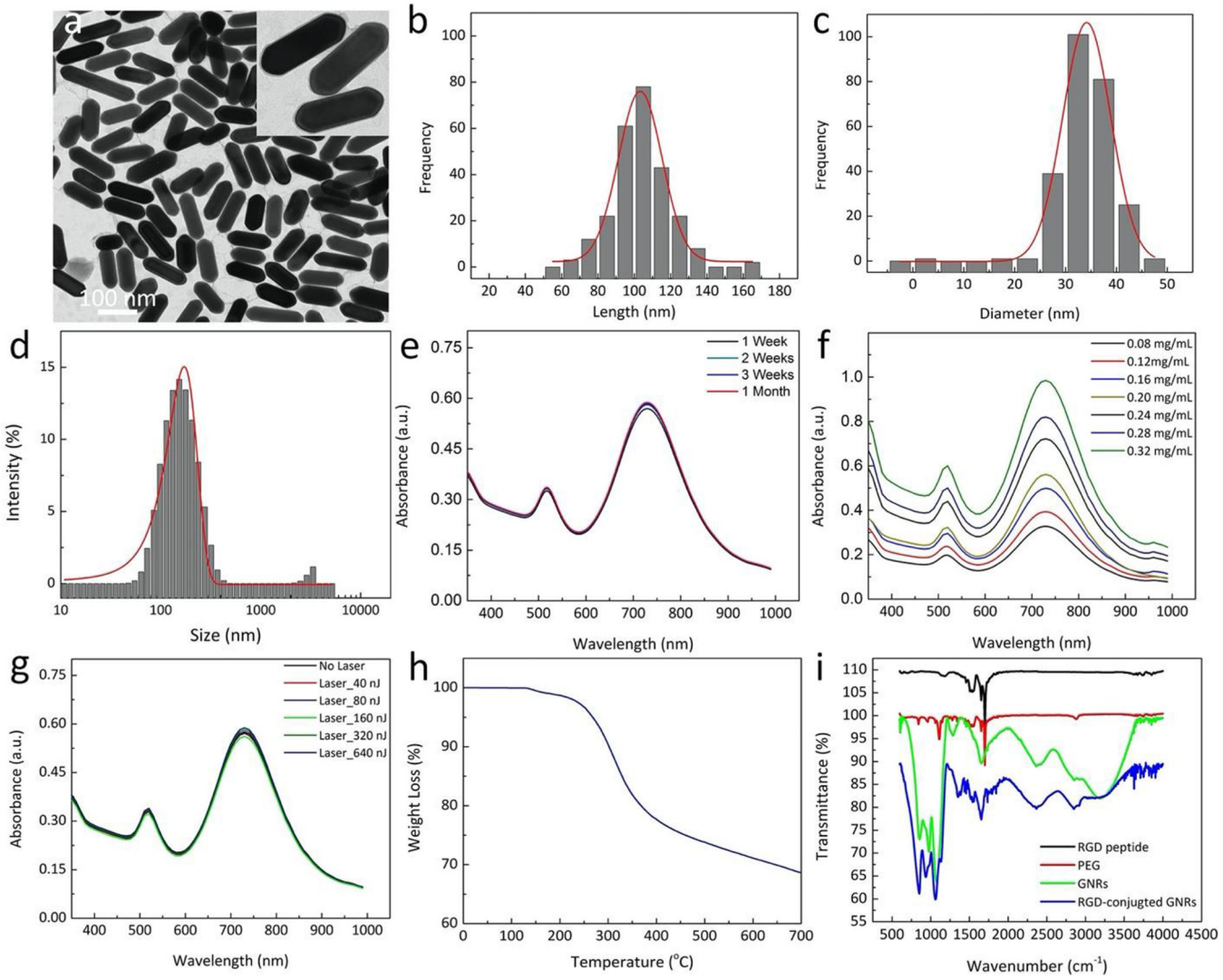

Figure 1. Characterization of functionalized gold nanorods (GNR):

(a) TEM image. Inlet image shows the morphology of single GNR. (b–c) Particle size distribution measured from 250 nanoparticles on the TEM image. The average size was estimated to be 34.17 ± 4.85 nm in width and 103.28 ± 12.07 nm in length. (d) Particle size distribution were obtained from dynamic light scattering (DLS) analysis with disperse index of 0.5. (e–f) UV-Vis absorption spectra GNR obtained at different time points (weekly for 1 month) and different concentrations (0.08–0.32 mg/mL) demonstrating biostability for at least 1 month. (g) Photostability of GNRs under pulse laser illumination at different energies from 0 to 640 nJ. There is no redshift of the absorption spectra, illustrating good photostability of GNRs up to 640 nJ. (h) A panel of thermogravimetric analysis (TGA) curves for GNR-RGD. (i) Fourier transformed infrared spectroscopy (FTIR) of PEG, RGD, bare GNRs, and GNR-RGD.

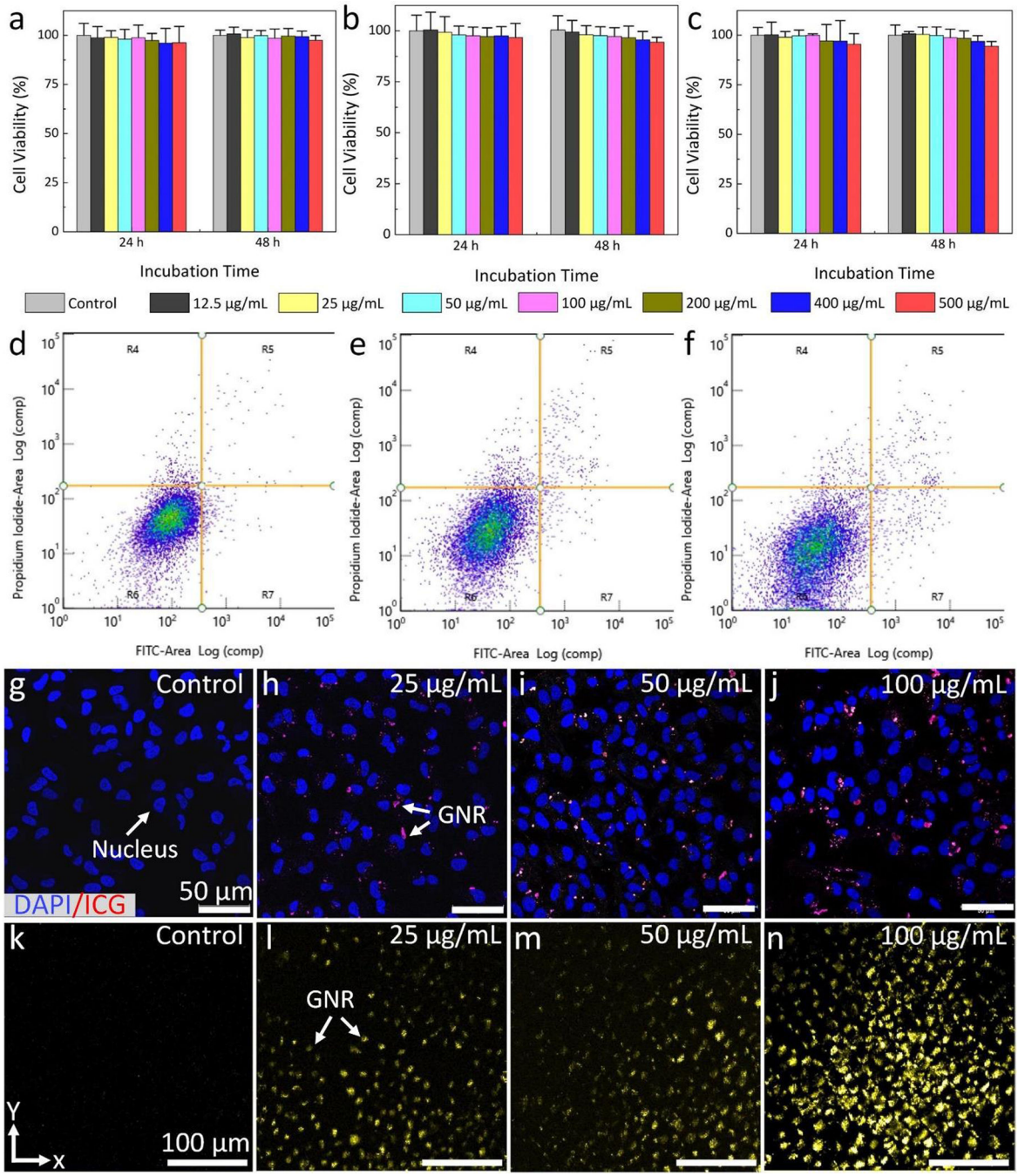

Figure 2. *In vitro* toxicity and cellular uptake of GNR:

(a–c) Cell viability of HeLa cells, bovine retinal endothelial cells (BRECs), and bovine brain endothelial cells (b.End 3) treated with GNRs at various concentration ranging from 0 (control) to 500 μg/mL and different incubation times (24 and 48 h), respectively. Most cells were viable even treated with GNRs at a high concentration of 500 μg/mL and long incubation time of 48 h. (d–f) Apoptosis and necrosis analysis of BRECs cells using flow cytometry. The flow cytometry was performed using Annexin V-FITC apoptosis detection kit protocol. (d) The untreated cells (control group). (e–f) BRECs cells treated with GNRs

at a concentration of 100 μg/mL and incubated for 24 h and 48 h, respectively. The inlet numbers indicate percentage of viable (R6), necrotic (R4), early apoptosis (R7), and late apoptosis (R5). (g–j) Confocal laser scanning microscopic images of the internalized GNRs in BRECs cells treated with GNRs at different concentrations: control (g), 25 μg/mL (h), 50 μg/mL (i), and 100 μg/mL (j). The treated cells were excited with HeNe laser at the optical wavelength of 640 nm. Blue fluorescent color indicates the morphology of nuclei stained by DAPI. Red fluorescent color shows the internalized GNR uptaken by cells. (k–n) Maximum intensity projection (MIP) PAM images of the treated BRECs cells acquired at the excitation wavelength of 700 nm. High contrast PAM was observed on the PAM image treated with GNRs at 100 μg/mL.

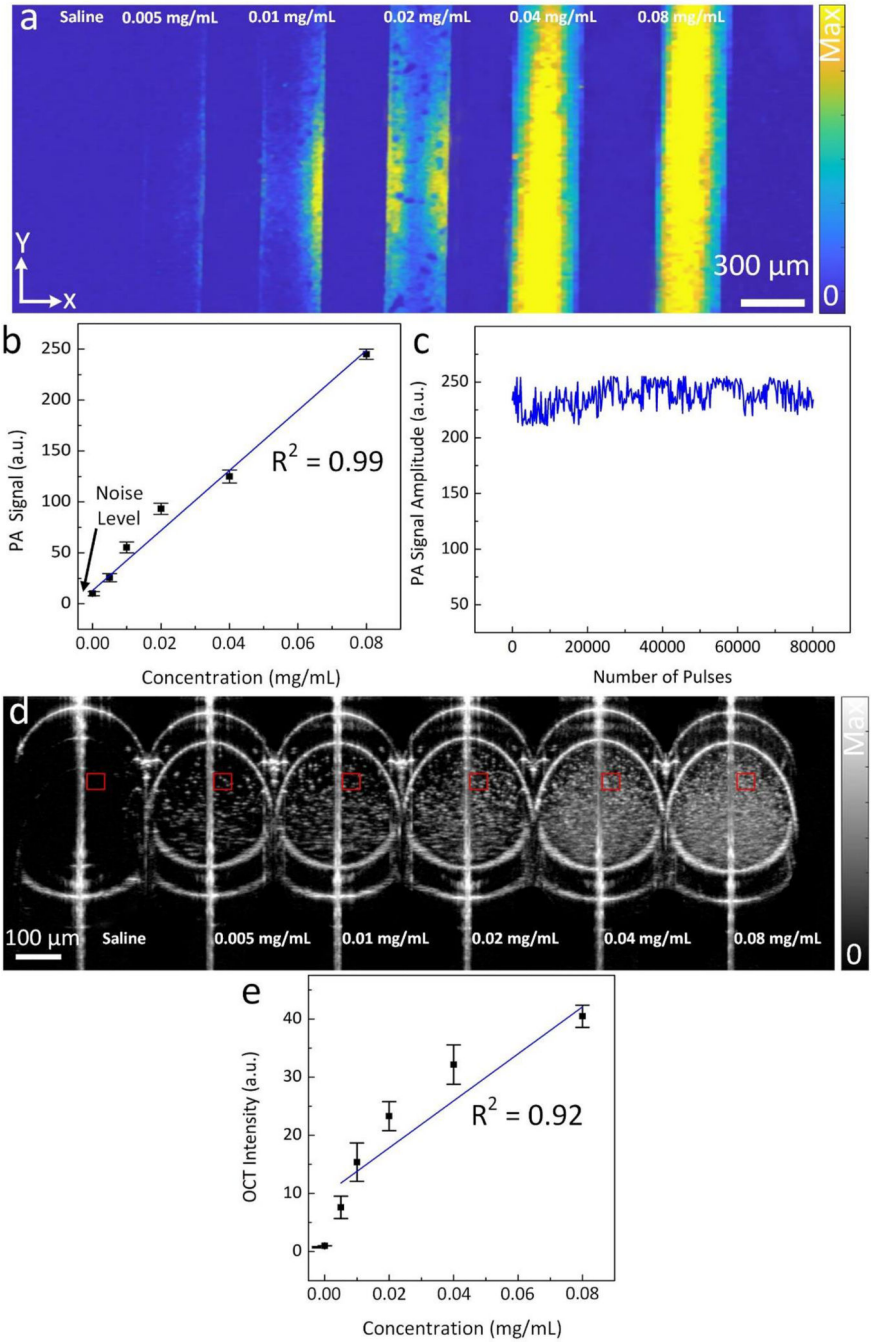

Figure 3. ***In vitro*** **PAM and OCT contrast evaluation of GNRs:**
(a) PAM images of silicone tube phantoms containing GNR suspension at multiple concentrations (0 (saline), 0.005, 0.01, 0.02, 0.04, and 0.08 mg/mL). The PAM images obtained at 700 nm using laser energy of 80 nJ.(b) Quantitative measurement PA signal amplitudes as a function of GNR concentration. The PA signal amplitudes were measured at three different regions of interest (ROI) on PAM images (N=3). The PA signal linearly increases with increasing concentration (R^2 = 0. 99, $p<0.05$). Black arrow indicates the background (BG) noise level. (c) Graph of PA signal amplitudes acquired during

illumination of 80,000 nanosecond laser pulses. The results show that the PA signal did not fluctuate significantly, indicating photostability of GNRs. (d) Cross-sectional B-scan OCT image of a group of glass capillary tubes filled with different GNR concentrations from 0 (saline) to 0.08 mg/mL. GNRs were clearly visible even at a low concentration of 0.005 mg/mL. (e) Quantitative measurement OCT signal intensities as a function of GNR concentration. The OCT signal intensity linear increased with the concentration of GNRs ($p<0.001$, $R^2 = 0.92$).

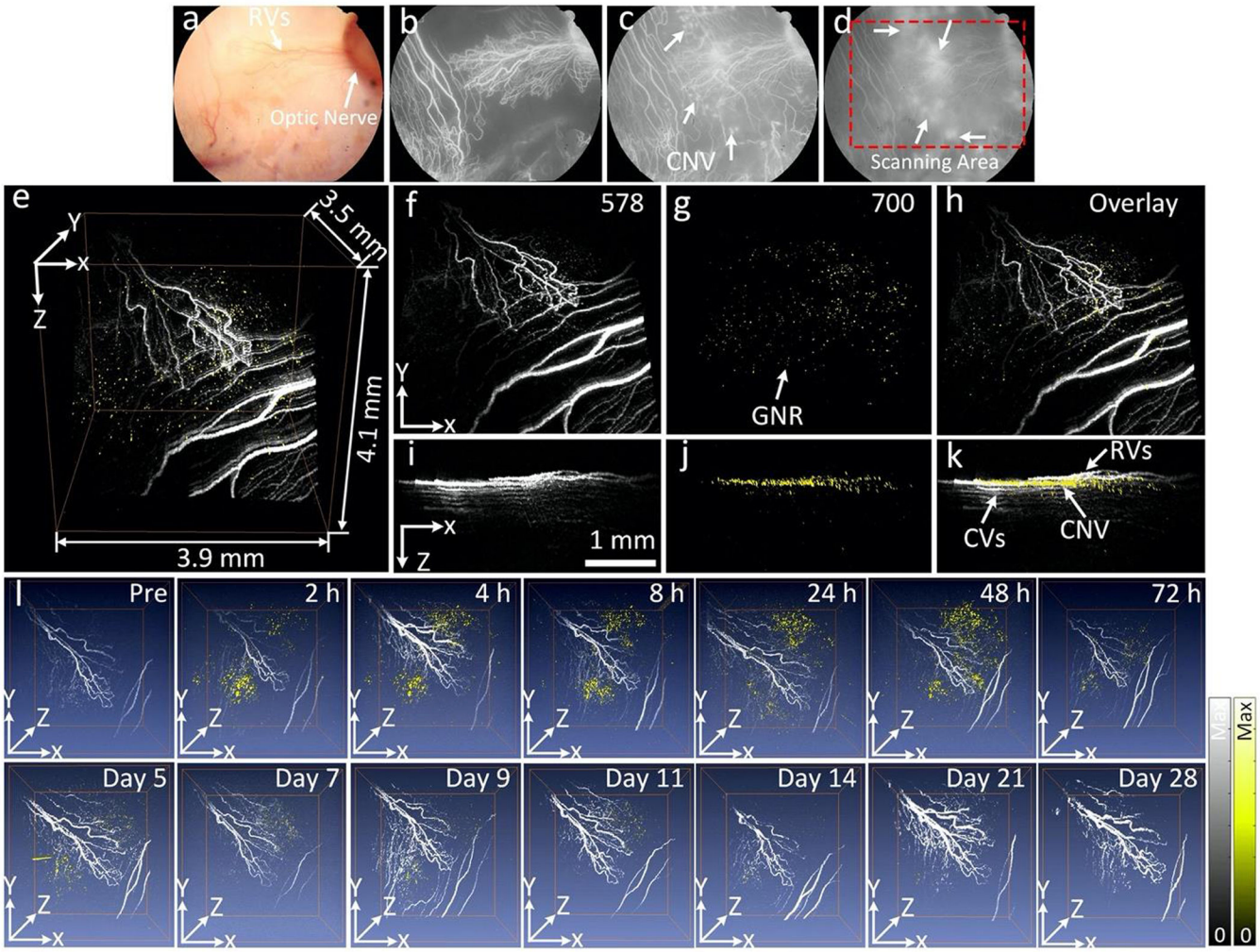

Figure 4. ***In vitro*** **PAM of targeted GNR in rabbit model of laser-induced choroidal neovascularization (CNV):**

(a) Color fundus photograph of the rabbit retina. The color fundus shows the retinal vessels (RVs) and optic nerve. (b–d) Fluorescein angiography (FA) images acquired at different time points after I.V. injection of fluorescein sodium: (b) early phase, (c) middle phase, and (d) late phase. The FA shows the morphology of retinal vessels, capillaries, and the location of CNV (white arrows). Red rectangle shows the selected scanning area. (e–k) Corresponding PAM images along the selected area outline in figure d obtained at two different excitation wavelengths of 578 and 700 nm. (e) 3D volumetric PAM visualization image (post 1 h). See Supplementary Visualization 2 for video representation. (f–h) Horizontal (x–y) MIP PAM images (post 1 h). (i–k) Vertical (y–z) PAM images (post 1 h). Pseudo yellow color represents the accumulation of GNRs in CNV. Noted that GNRs were laid under retinal vessels and above the choroidal vessels (k). (l) Sequential longitudinal *in vivo* PAM images (overlaid 3D images acquired at 578 and 700 nm) acquired on the same rabbit at various time points post administration of targeted GNR-RGD (0.4 mL, 2.5 mg/mL) and followed sequentially for 28 days.

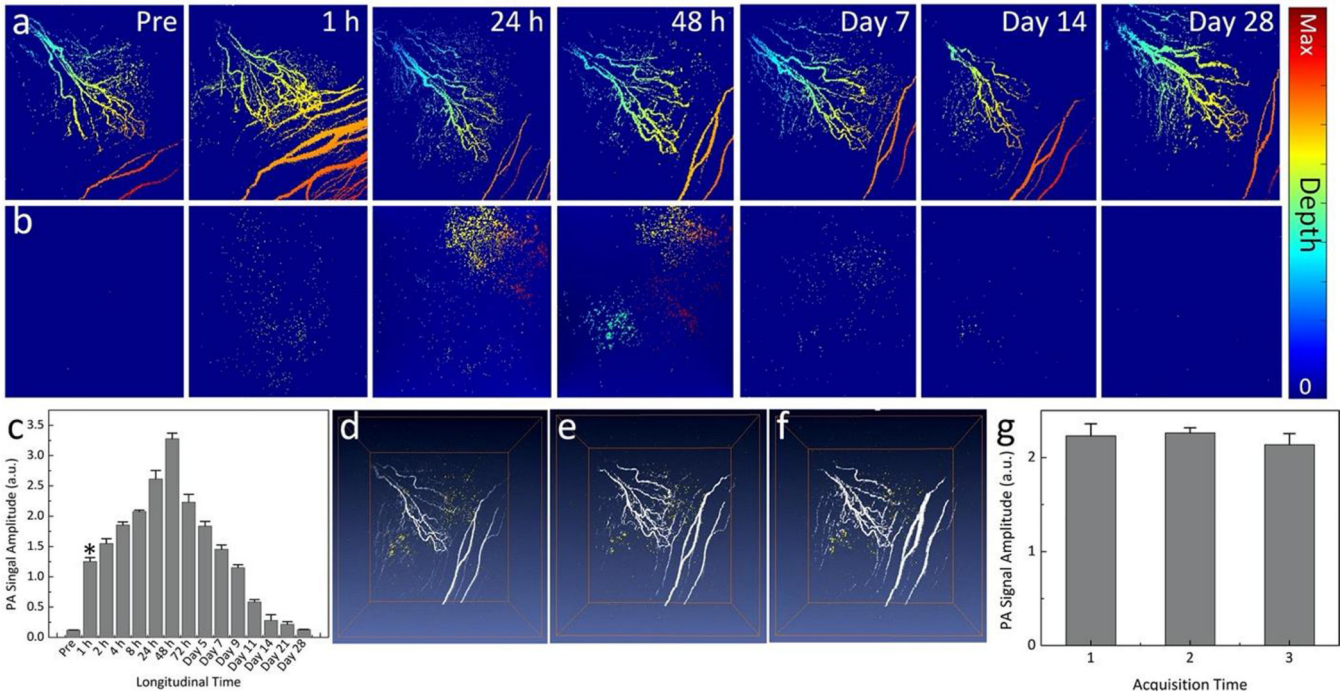

Figure 5. Depth and *in vivo* photostability of targeted GNR-RGD:

(a–b) Selected depth- encoded PAM images (x–y MIPs) acquired at 578 nm (a) and 700 nm (b), respectively. These images show the retinal vessels (RVs), choroidal vessels (CVs), and CNV located at different depths. (c) Graph of the quantitative PA signal amplitudes as a function of times. Peak PAM signal occurred at 48 h post-injection. (d–f) Overlay 3D PAM images acquired at 578 and 700 nm at different scanning times: First scan (d), second scan (e), and third scan (f). The PAM signal amplitudes fluctuated slightly about 5.5 % (PA_{Signal} = 2.23 ± 0.13 (a.u.), 2.26 ± 0.06 (a.u.), and 2.14 ± 0.12 (a.u.) for the first, second and third scan, respectively).

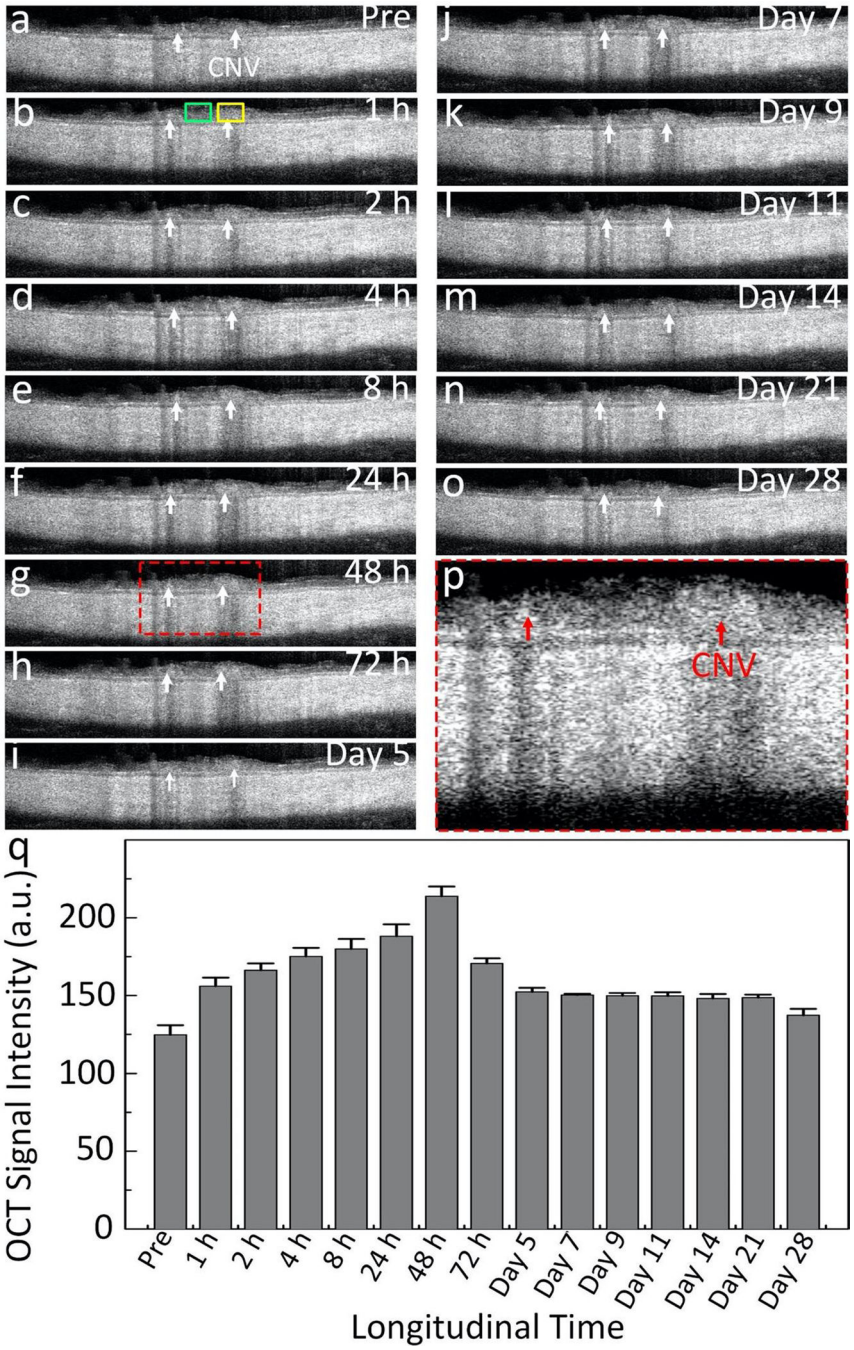

Figure 6. ***In vivo*** **OCT images of targeting GNRs:**

(a–o) Longitudinal B-scan OCT images achieved pre- and post-injection of GNRs over a period of 28 days. CNV were visualized after the injection (white arrows). (p) Magnification of the selected region of interest shown in Figure 6g. Red arrows show the surface margin of CNV. (q) Graph of the measured OCT intensity at CNV isolated from the acquired OCT images using regions of interest (ROI) as a function of the injection times. ROIs were selected at the position of CNV (yellow rectangles) and adjacent tissues (green rectangles). The OCT signal increased at a peak of 171.4% at 48 h post injection.

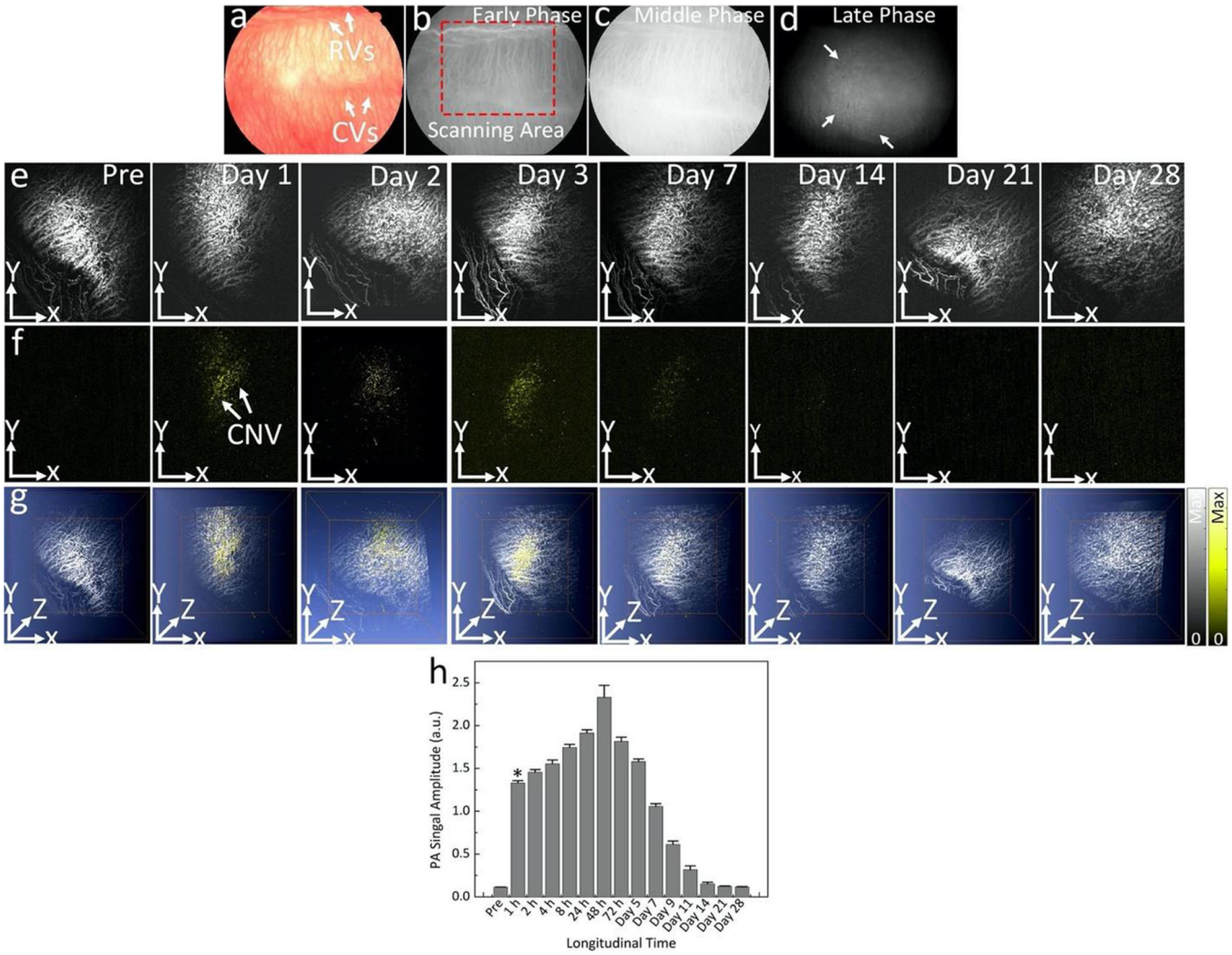

Figure 7. ***In vivo*** **PAM images of targeted GNRs in a CNV rabbit model using subretinal injection of VEGF-165:**

(a) Color fundus photography of the rabbit model. (b–d) Early, middle and late phase indocyanine green angiography (ICGA) images, respectively. White arrows provide an indication of the growth of CNV. (e–g) x–y MIP and overlay 3D PAM images acquired at 578 and 700 nm pre and post-injection at day 1, 3, 7, 14, 21, and 28. Pseudo yellow color on the PAM images acquired at 700 nm provide an evidence of the distribution of GNRs around the CNV. Note that there was no signal observed on the PAM image before the injection. (h) Quantification of PAM signal amplitudes of GNRs over time for 28 days. The PAM signal amplitude of GNRs increases post-injection and peaked at 48 h. Then, the PA signal gradually decreases over time.

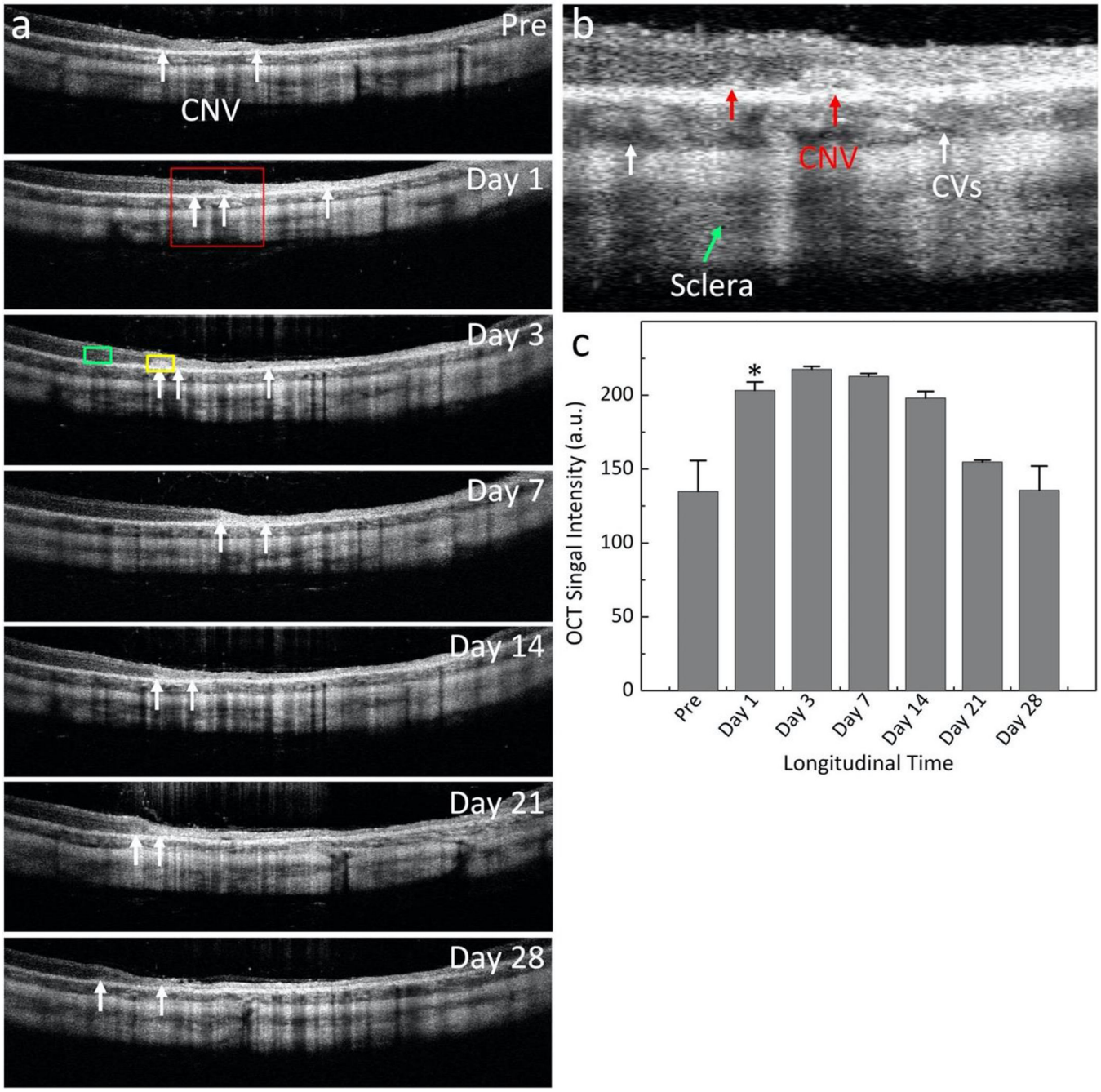

Figure 8. ***In vivo*** **OCT images of targeted GNR in CNV rabbit model using subretinal injection of VEGF-165:**

(a-b) Long-term B-scan OCT images acquired before and on day 1, 3, 7, 14, 21, and 28 post I.V. injection of GNR. The white arrows indicate the location of CNV. Yellow and green rectangles show the selected region of interests (ROIs) to determine average OCT signal intensity at the position of CNV and adjacent tissues, respectively. (b) Magnification of the selected region outlined in Figure a. The surface margin of CNV was observed (red arrows) along with different layers such as choroidal vessels (CVs), and sclera. (c) Graph of OCT

intensity versus injection time, showing the increase of OCT signal which peaked at 161.3% at day 3 post-injection.

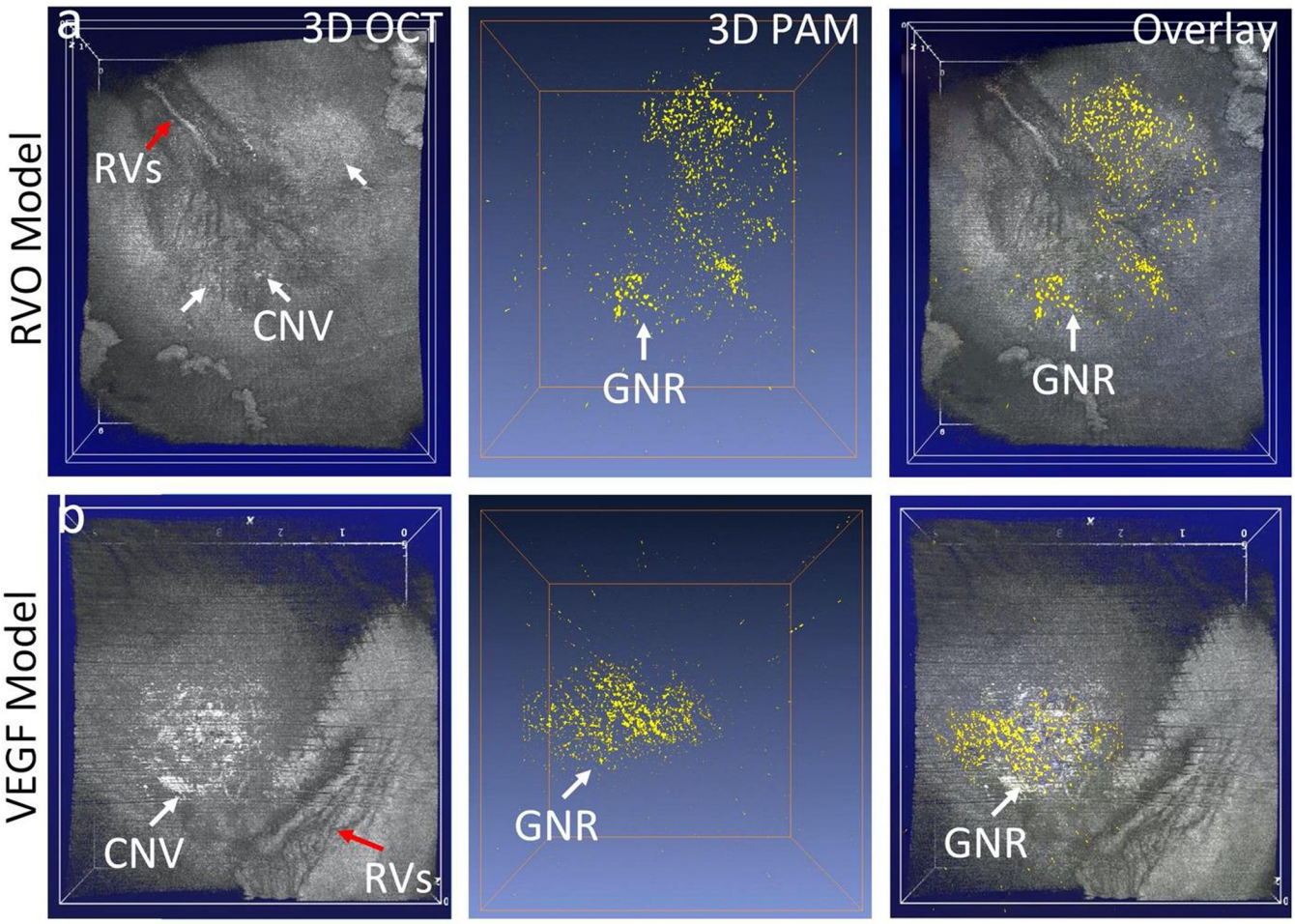

Figure 9. Fusion *en-face* volumetric PAM and OCT images.

(a) RVO induced CNV model. (b) Subretinal injection of VEGF model. Red arrows show the morphology of retinal vessels (RVs). White arrows show the developed CNV with high contrast on 3D OCT images. 3D PAM image obtained at 700 nm. Overlay PAM and OCT shows the distribution of GNR binding at CNV.

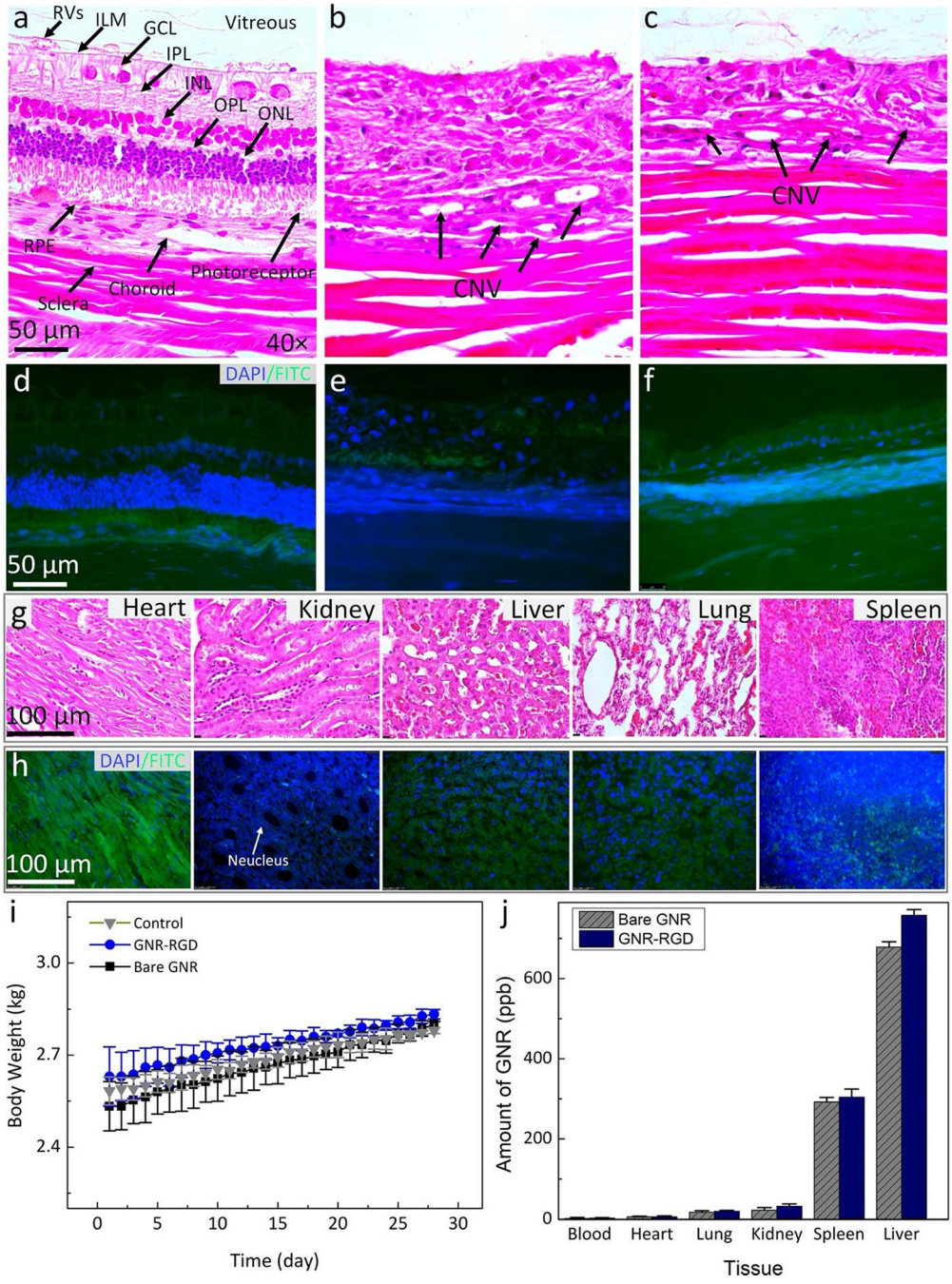

Figure 10. Histological analysis and TUNEL assay after GNR injection in rabbits:

Hematoxylin and eosin (H&E) images of the control (a), laser-induced CNV model (b), and subretinal injection of VEGF-165 (c). The control image shows different layers of the retina such as retinal vessels (RVs), internal limiting membrane (ILM), ganglion cells layer (GCL), inner plexiform layer (IPL), inner nuclear layer (INL), outer plexiform layer (OPL), outer nuclear layer (ONL), photoreceptors, retinal pigment epithelium (RPE), choroid, and sclera. The treated tissues show evidence of the development CNV (black arrows). In addition, a significant change in retinal thickness was observed. However, there were no

specific changes in cell morphology related to the administration of gold nanoparticles. (d–f) TUNEL staining of treated tissues with GNR with different groups. The green fluorescent color indicates the TUNEL-positive cells detected in each group. Blue fluorescent color represents cell nuclei stained with DAPI. (g–h) H&E and TUNEL staining of different organs (*i.e.*, heart, kidney, liver, lung, and spleen). There is no tissue disorganization observed on H&E and no TUNEL-positive cells detected on these samples, confirming that GNR-RGD induced minimal systemic toxicity. (i) A graph of body weight measured from three treated groups (control, treated with bare GNR, and GNR-RGD). (j) Biodistribution of GNR in organs post administration of GNR and GNR-RGD. Most GNR accumulated in the spleen and liver.

Table 1:

Liver and Kidney Function Tests in Rabbits

Test	Unit	Normal Range	Control	Treated with GNR	Treated with GNR-RGD
Creatinine	mg/dL	0.5–2.6	1.63±0.80	2.20±0.31	1.76±0.68
Albumin	g/dL	2.7–5	3.73±0.47	3.70±0.80	4.53±0.91
Total Protein	g/dL	5–7.5	6.17±0.91	6.37±1.10	5.97±0.96
Alanine Transaminase	U/L	25–65	50.33±14.57	52.00±13.08	60.00±2.00
Total Bilirubin	mg/dL	0.2–0.5	0.08±0.01	0.23±0.04	0.13±0.05
Blood Urea Nitrogen	mg/dL	5–25	20.33±6.43	18.67±5.03	21.67±2.52
Alkaline Phosphatase	U/L	10–86	73.33±11.59	67.33±10.07	81.67±2.52